Til Unni

Acknowledgements

The work on this thesis has been carried out at the Department of Chemistry at the Norwegian University of Science and Technology (NTNU), with funding from the Norwegian Research Council and NTNU. There are several people I would like to thank for their friendship and help during the work on this thesis. It would have been impossible to carry on through these two years without these people.

First I would like to thank my supervisors Prof. David G. Nicholson and Dr. Karina Mathisen for their guidance, and for all the support and wise advice they have given me. I could never have asked for better supervisors, and I am very grateful for the opportunity to work with them. Thank you both for inspiration and good humor these past two years.

There have been several people helping out with the practical execution and training in the methods used in this thesis. I would like to thank Syverin Lierhagen for carrying out the ICP-MS analysis for me, and Julian “Jools” Tolchard for his training in SEM and BET (and for his amusing wittiness during these lectures). Also, I would like to thank the staff at ESRF for the rigging and fixing of the equipment prior to the experiments. In addition, I would like to thank Lillian Hanssen for her help with the administrative planning of the Master’s Degree and helpful advice about choice of subjects.

I would like to thank my fellow students; Anlaug, Asmira, Beate, Katrine, Mari and Tina. We have had a lot of fun these past two years, and we have faced the challenges together. I would never have made it without the team spirit and friendship we have had. Especially I would like to thank Anlaug for the “good” humor and many laughs we have had together, which have carried me through the hard times. Dr. Camilla Nordhei has been of great help when I was in need for advice about XAS analysis, and I appreciate our heated discussions about whom of us gets Aragorn (he’s mine, by the way…). Also, I would like to thank Christer L. Øpstad for his help with the formulation of the structure of silver sulphate.

Also there are other friends I would like to thank for their support and encouragement. I could give a long list of great friends, however I especially want to mention Ingrid, my flat mate, and Ann Marit, my best friend from back home. They have both been there for me when I’ve needed a pep talk or someone to share joys and sorrows with.

I would like to express my gratitude to all the people at “Mandagspilsen” at Den Gode Nabo; you have given me a place of refuge. We have had many great laughs, and I have very much enjoyed solving the Problems of the World over a beer (or several).

The most important people I would like to thank is my family; Mom & Bernhard, Dad, Halvor and Ola. They have always been supportive and proud of me, regardless of what I have chosen to do with my life. They have given me strength to go on, even when all seemed hopeless. I love you all, and I wish that my very much loved and greatly missed stepmom, Unni, could have been here with us to celebrate, and experience this milestone in my life.

And at last (but not least) I would like to thank my boyfriend Irvin, for his patience with me when I have been stressed out and for helping me out with the layout, references and proofreading of the thesis. He has read it over and over to help me make it better, and I am ever grateful for his help. Thank you for being my pedestal in life, and for always cheering me up. I love you.

Mari Kirkebøen Næss,

Trondheim, May 2009

Table of contents

Introduction

Microporous crystalline aluminiumphosphates (APO_4-*n*’s) and silicoaluminiumphosphates (SAPO-*n*’s) constitute an important group of inorganic materials because of their high potential as adsorbents and heterogeneous catalysts [1]. Transition metal incorporated $MeAPO_4$-*n*’s and MeSAPO-*n*’s have received much attention due to their potentially catalytically active nature. It has been claimed that a variety of transition metal ions (Me=Co, Mn, Zn, Ni, Cr, Ti, Fe, Cu, Cd, V) have been incorporated into the framework of the microporous structure by isomorphous substitution, thus changing the properties of the microporous material [2]. These catalysts are interesting for several heterogeneous catalytic reactions such as oxidation, acid catalysed reactions, isomerisation and selective catalytic reduction of NOx [2]. However, no reports on silver incorporated APO_4-*n*’s and SAPO-*n*’s have been found. Silver is an interesting transition metal regarding catalysis, because of its unique redox properties. It is well-established that Ag/Al_2O_3 is among the most active and selective catalysts for selective catalytic reduction of NOx with hydrocarbons (HC-SCR) [3], where the selectivity of the process is dependent on the morphology and state of the silver [4].

This thesis considers the possibility of incorporating silver into the framework of a microporous crystalline material, thus hydrothermal syntheses of $AgAPO_4$-5 and AgSAPO-11 have been performed. However, as the silver(I) ions were reduced to silver(0) metal prior to the crystallization of the framework, the thesis was expanded to involve silver(I) ion exchanged SAPO-*n*’s, in order to investigate growth of silver nanoclusters.

Several techniques have been used to characterize the samples in this thesis. X-ray diffraction data has been collected to fingerprint the crystal structure of the synthesised samples, and Inductively Coupled Plasma Mass Spectrometry (ICP-MS) has been used to investigate the silver content and the molar composition of the samples. Thermogravimetric analysis (TGA) has been performed to investigate the thermal stability of the samples, and to investigate exothermic and endothermic reaction as the templates (elaborated in the theory section) goes off. Scanning Electron Microscopy (SEM) and Transmission Electron Microscopy (TEM) images have been collected in order to investigate the morphology of the samples, and to measure the cluster size, respectively. The surface area of the samples has been examined with the Brunauer–Emmett–Teller method (BET) in order to determine the porosity of the samples, and investigate whether the presence of silver in the structure alters the available surface area.

However, the most important technique used in this thesis is X-ray Absorption Spectroscopy (XAS). This technique gives information about the local environment surrounding the silver, giving the opportunity to decide whether the silver is incorporated into the structure, or if it is in an extraframework position. Knowledge of the positions and character of the metal ions in the microporous carrier can give insight into the function of the catalyst. In order to make a high-quality catalyst, it is important to understand the role of the active metal to be able to optimize the process [5]. XAS gives an opportunity to estimate the size of metal clusters, which is interesting due to the differing properties of small metal clusters, opposed to the metal bulk. When silver clusters become very small (< 20 Å) their properties change [6] and they can become active sites in a catalyst. Silver(I) exchanged SAPO-*n*'s can be exposed to a reducing atmosphere with the intention that the silver(I) ions are reduced to metallic silver(0). Finding the size of these nanoclusters can give information about where they are; if the clusters are small, they may be inside the pores of the SAPO-*n*, restricted from growing, and if they are large they are most likely present on the external surface of the SAPO-*n* particles. XAS gives a unique opportunity to investigate this, due to the possibility of *in-situ*[1] experiments.

---

[1] *in-situ* is Latin for “in the place”

Theory

2.1 Microporous crystalline materials

Microporous crystalline materials, also referred to as molecular sieves[2], have received much attention, due to their unique abilities as catalysts and as carriers of active substances for catalysis. From nature we know zeolites (aluminiosilicate) to be microporous crystalline materials, and many attempts have been made to copy their structure. In 1982, Wilson et al. reported to have synthesized microporous molecular sieves made of AlO_4 and PO_4 tetrahedra linked together; Aluminiumphosphates ($AlPO_4$-*n* or APO_4-*n*) [7]. They made several types of structures, some of them analogues to natural zeolites, e. g. $AlPO_4$-42 (zeolite A structure), $AlPO_4$-34 (chabazite) and $AlPO_4$-37 (fajuasite). The number *n* in $AlPO_4$-*n* denotes the structure of the material, which is sometimes referred to as *zeotypes* [8]. These materials have a neutral framework, thus no ion exchange capacity [9].

$AlPO_4$-5 and $AlPO_4$-11 are unique synthetic structures with no analogues within the natural zeolites. The $AlPO_4$'s are made by mixing an alumina source and a phosphorous source, usually ortho-phosphoric acid, to make a synthesis gel. A structure directing agent (template) is added to the gel to obtain the pores in the structure. The template is usually an organic compound, such as i-diisopropylamine (i-Pr_2NH) or N-methyl dicyclohexylamine (MDCHA). Subsequently the synthesis gel is hydrothermally treated at 100-250°C to obtain the crystallization of the structure [7]. If a source of silica is added in the synthesis gel, some of the phosphorous ions (+5) will be substituted with silicon ions (+4), and thus the lattice will obtain a net negative charge which is balanced with H^+-ions. These silicon-substituted $AlPO_4$-materials are called silicoaluminiumphosphates (SAPO-*n*), and their structures follow that of $AlPO_4$ materials, so that a SAPO-5 possesses the same structural framework as $AlPO_4$-5 [9]. In this thesis, $AlPO_4$-5, SAPO-5 and SAPO-11 have been synthesized and studied, and their structures are shown in fig. 1. The structure of APO_4-5 consists of 12-, 6- and 4-ring channels, interconnected by windows of 6-rings. The biggest channel is the main channel, and the diameter of this almost circular pore is 7.3 Å. The SAPO-11 structure is built from 10-, 6- and 4-ring channels, and the elliptical 10-ring channel is 6.4×4.0 Å [9].

---

[2] Molecular sieves; because their structure allows only small molecules to pass through, and molecules too large are sieved out [11].

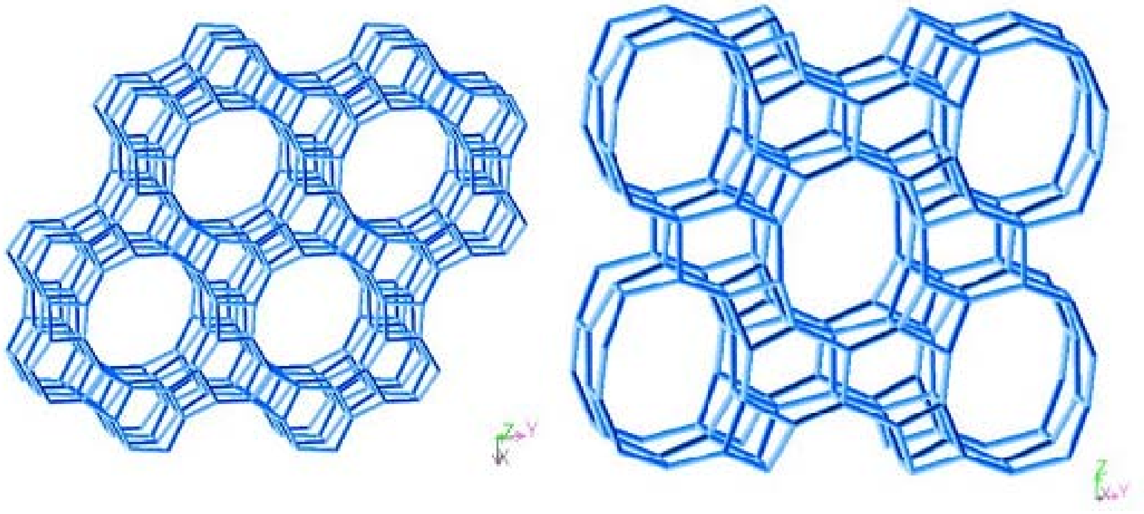

Figure 1: *The left image is an illustration of the structure of APO$_4$-5, and on the right is a SAPO-11 structure [10].*

An important and interesting property of these materials is their ability to replace one of their metal ions with other metal ions, to make MeAPO$_4$-*n*. This isomorphous substitution alters the properties of the material, and can make it catalytically active. To incorporate a metal into the AlPO$_4$-*n* framework, it is necessary to add the metal salt to the reaction mixture prior to the crystallization, and both Al(III) (0.39 Å) and P(V) (0.17 Å) can be substituted [1]. Of special interest to many researchers are transition metal incorporated AlPO$_4$'s and SAPO's. It is believed that the transition metals can incorporate into the actual framework, thus making the material catalytically active by e.g. Brønsted acid sites, see fig. 2. Substitution into a framework usually requires that the substituting cation has similar size and coordination requirements as the substituted ion; however, the APO$_4$-*n* framework is quite flexible, thus it is possible to substitute the relatively large transition metal ions into the framework [2]. SAPO-*n* is different however, because they possess the ability to be ion exchanged [9]. The metal can be introduced by ion exchanging with an aqueous solution of the metal ion to be incorporated. The compounds are then detonated Me:SAPO-*n*, and the introduced metal ions are fixed at a cation site, which give them an extraframework position in the structure (like the H in fig. 2) [2].

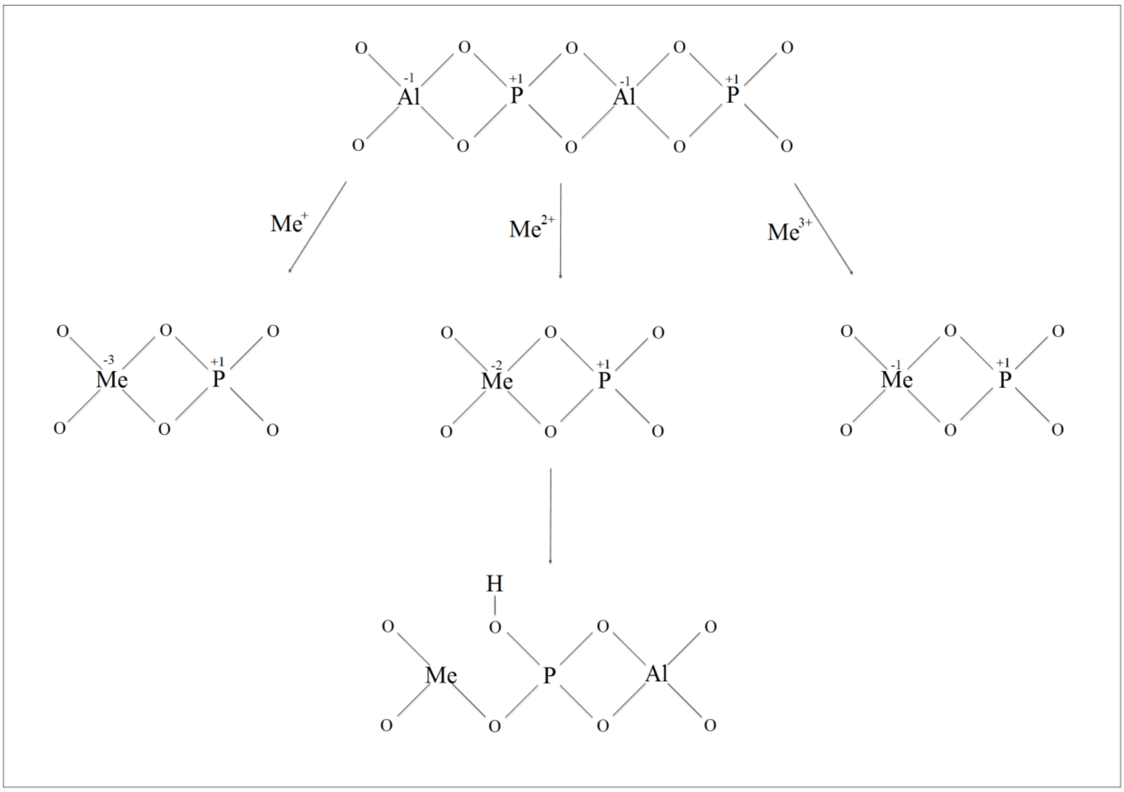

Figure 2: *The substitution of Al(III) with Me(I), Me(II) and Me(III) metal ions, and an example of Me(II) substitution leading to the formation of Brønsted acid sites.*

Microporous crystalline materials are different from the conventional oxide carriers of metal clusters (e.g. Al_2O_3 and SiO_2), due to their three dimensional framework giving both external and internal surface where the metal clusters can be present. When the introduced metal ions are ion exchanged into the SAPO-*n* framework, they can be exposed to a reducing environment and thus become metal clusters trapped inside the pores of the zeotype. Due to their small size, the pores will stabilize the clusters and restrict them from becoming too large or sintering together to agglomerates. These steric restrictions are useful to make highly dispersed metal catalysts [11].

There are several features with the zeotypic material that are interesting within heterogeneous catalysis. Due to the size of the pores, the molecular sieves are size and shape selective [7], thus they can be used as catalysts in selective reactions. In addition, the pores in the structures provide a large inner surface, which gives the material adsorptive properties [1]. An additional property of $AlPO_4$'s is that they are thermally stable. The crystallized *as-synthesised* product has to be calcined in air to burn off the organic template, and thus make the channels and voids in the framework available for adsorption or catalysis. This calcination usually takes place in air at 400-600°C, without any collapse of the lattice [7].

This property makes the material suited for catalysis at high temperature, as for instance removal of NO in exhaust gases from cars or other combustion processes.

2.2 Silver and its properties

Silver is a second row transition metal, and is the 47th element in the Periodic Table. Silver has an electronic configuration of $1s^2$ $2s^2$ $2p^6$ $3s^2$ $3p^6$ $4s^2$ $3d^{10}$ $4p^6$ $5s^1$ $4d^{10}$, which makes it easy for the metallic silver (Ag^0) to lose an electron, $5s^1$, to become a relatively stable ion (Ag^+). Compounds containing silver(I) ions are sensitive to light, because UV-radiation will lead to photo reduction of the ions into metallic silver(0). Silver can also exist in the oxidation states Ag(II) and Ag(III). The divalent silver can readily be made and stay in a rather stable aqueous solution if the solution is strongly acidic with a non-reducing acid. The Ag(II) species are paramagnetic, due to the unpaired electron in $4d^9$, and the solutions tend to be coloured, with the colouring depending on the acid used in the solution. The AgO compound has been suspected to consist of a mixture of Ag(I) and Ag(III), and not Ag(II) which it was first believed to be. This is due to the low magnetic susceptibility found for the compound. Both Ag(I) and Ag(III) are diamagnetic, and the existence of two kinds of silver has been confirmed by neutron diffraction, but the nature of argentic oxide is not fully understood. The Ag(III) specie can only exist as a complex with fluorine ligands (F^-) or organic ligands [12].

Silver lies between copper and gold in the IB series in the Periodic Table, yet its physical properties exhibit anomalous values rather than values which fall between those of copper and gold, e.g. thermal conductivity, melting point and boiling point. Metallic silver exhibits the highest thermal and electrical conductivity of all the elements, and is the most reactive “noble” metal. Silver is not oxidized by oxygen at room temperature, but a thin oxide layer can be formed at 200°C. Silver(I) ions have a high polarizing power, due to the weak shielding from the filled d-orbital. Thus the attractive forces from the nucleus to the extranuclear electrons give a small ionic radius (1.26 Å). This effect gives silver(I) ions a strong tendency towards complex formations [12]. Silver(I) easily form complexes with organic amines, to form stable silver-amine complexes [13]. As the templates used in the syntheses of zeotypes usually are amines, this may cause a problem for the hydrothermal incorporation of silver into the framework. The silver complexes formed with primary amines are more stable than complexes with secondary amines, which in turn are more stable than tertiary amines. This is due to steric hindrance in the silver-amine system [13].

The thermal stability of silver(I) salts are varying; silver(I) oxide is reduced upon heating as evolution of oxygen begins at about 160°C and becomes rapid at 260°C. Also silver(I) acetate decompose to the metal upon heating, however silver (I) nitrate is stable in air up to ~350°C, but at 440°C it decomposes completely into the metal [12]. Thus silver(I) ions are relatively thermally unstable, and will readily be reduced to silver metal upon heating.

Research have been performed on how the properties of silver(0) changes when the size of the particles become very small. In bulk metal, silver has an fcc structure, with a multiplicity of 12 and a Ag-Ag bond length of 2.889 Å [12]. These are all properties that change when silver is in the form of small nanoclusters. Clusters composed of only a few atoms can be considered small molecules (dimers, trimers etc.), while nano- and microclusters are small aggregates of atoms with properties considerable different from the bulk [6]. When the clusters become smaller than 20 Å in diameter, contraction of the bonding distance and a decrease in the multiplicity can be observed. Because the surface atoms embody a large fraction of the material in nanoclusters, they will be in a strained condition, and which cause the lattice to contract due to high surface energy. George et al. (1992) studied silver aggregates of 20 nm in size, and they report a contraction of the lattice constant of 15%, without any drastic change in the crystal structure (fcc-lattice) [14]. Xu and Kevan (1991) report to have formed silver clusters by H_2-reduction of silver-exchanged zeolite rho, and estimated a Ag_4^{n+} (n= 1or 3) cluster to have a diameter of 5.4 Å. They observed an interesting property of these tiny clusters; the reduction and oxidation of the silver clusters are reversible, and they seem to be able to migrate into the zeolite cages as they are being reduced, and in the oxidation process the cations migrate back to cation sites in the negatively charged zeolite framework [15]. These can be interesting properties within e. g. catalysis.

The redox properties of silver are interesting in many ways, especially within catalysis, and there have been performed some research on silver as a possible active component in catalysis. Shimizu et al. (2001) found that highly dispersed silver on alumina (Ag/Al_2O_3) are predominantly present as Ag^+ species when the silver content is below 2 wt%, and that this catalyst has the ability to selectively reduce NO with hydrocarbons to N_2. At higher silver loadings they reported the silver in the form of Ag_n being responsible for non-selective hydrocarbon combustion and N_2O formation [16]. Shibata et al. (2004) performed a selective catalytic reduction (SCR) of NO in the presence of hydrogen, using a

Ag zeolite as a catalyst. They report that the exchanged Ag^+ components probably are transformed into Ag_4^{2+}, due to the H_2 present in the reaction gas mixture, and that these ionic clusters are responsible for the SRC of NO by propene [17].

2.3 X-ray absorption spectroscopy

X-ray absorption spectroscopy is a powerful analytical tool in research. The increasing availability of synchrotron radiation sources in the last three decades has made the method applicable in several disciplines. It is an important technique for structural analyses of compounds of many sorts.

The technology is based on electrons interacting with the element being investigated, and a simple sketch of the synchrotron radiation source is displayed in fig. 3. Electrons are first accelerated from a linear accelerator and injected into a booster ring which increases the rate of the electrons. The high-speed electrons, with velocities up to the speed of light, are then sent into the storage ring which contains homogenous magnetic fields made by bending magnets. The magnets change the direction of the electrons and make them move in a circle. When charged particles change the direction of their velocity, they will lose energy in the form of photons. This is a continuous spectrum of photons, called white light, and the beam is sent through a monochromator which single out the chosen energy of the X-rays to be used in the transmission experiment. Subsequently, the monochromatic X-ray is sent to the hutch where the transmission experiment is carried out, and behind the hutch is a control room where the personnel reside to control the experiments [18; 19].

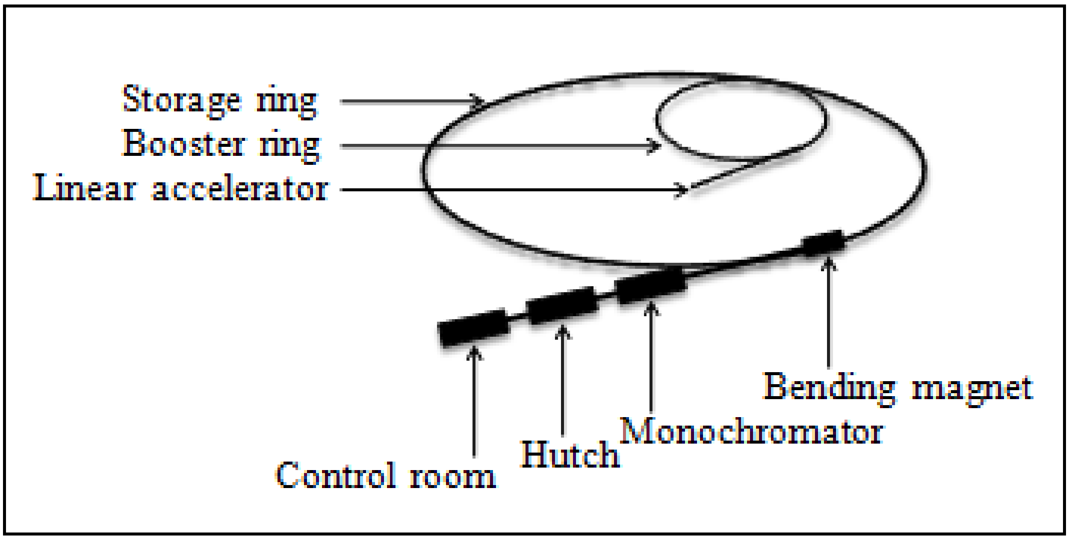

Figure 3: *Sketch of a synchrotron radiation source.*

When the monochromatic beam strikes the sample in the hutch, a photon from the X-ray beam hits the absorbing atom and kicks out one of the core electrons, which turn into a photoelectron. The photoelectron spreads out like a spherical wave, and is scattered by the neighbouring atoms (backscatterers), and constructive and destructive interference between outgoing and backscattered waves arise. The course of action is sketched in fig. 4.

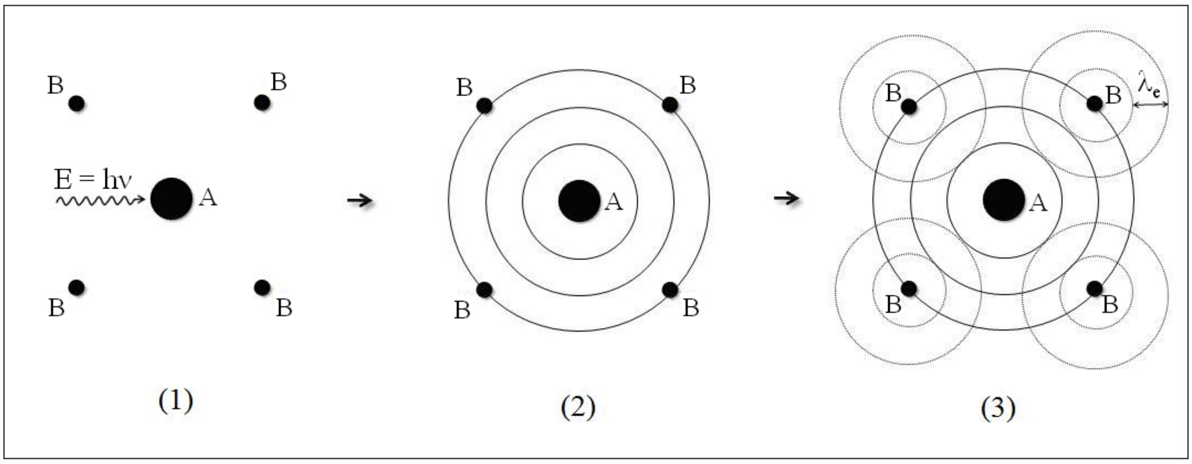

Figure 4: *A basic explanation to XAS. (1): The incoming photon with energy E = hν hits the absorbing central atom, A. (2): The photoelectrons from A spreads out as spherical waves (solid lines) and hits the backscatterers, B, and (3): the B-atoms backscatter the photoelectrons, hence interference arises between the outgoing and the backscattered waves (dotted lines). The waves have a wavelength* λ_e.

The minimum energy of the photon necessary to eject one of the core electrons is the *threshold* energy (E_0), and corresponds to the binding energy of this particular electron. This energy is characteristic for each element, and is called the absorption edge [18; 19].

2.3.1 Theory of Extended X-ray Absorption Fine Structure (EXAFS)

The EXAFS theory is based on the approximation that the photoelectron is backscattered once by a neighbouring atom placed at a short distance from the absorbing atom (*short-range single-electron single-scattering theory)* [18]. As the beam of monochromatic X-rays travel through a material, it will lose some intensity due to interaction with the matter. This relationship can be expressed as

$$dI = -\mu I dx \tag{1}$$

where *I* is the original intensity, μ is the linear absorption coefficient and *x* is the thickness of the sample. Integrating eq. 1 gives

$$\frac{I_t}{I_0} = e^{-\mu x} \tag{2}$$

where I_0 and I_t are the incident and transmitted intensities, respectively, of the X-rays travelling through a material of thickness *x*. In an experiment, the μx is calculated by

$$\mu x = \ln \frac{I_0}{I_t} \tag{3}$$

The absorption K-edge occurs when the energy of the incoming X-ray has the energy corresponding to the binding energy of the 1s electron of the absorbing atom. The absorption coefficient, μ, will show an immediate increase at this energy, see fig. 5 (it is called the K-edge because the 1s electrons are in the K-shell. If the electron being emitted is 2s, $2p_{1/2}$ or $2p_{3/2}$ (L-shell), the edges that occur are L_I, L_{II} or L_{III}, respectively) [18].

If an isolated atom is the one studied, the absorption spectrum will be smooth after the edge and decrease gradually with increasing energy. This is because the spherical wave of the photoelectron will move unhindered without being scattered by any neighbours. However if the absorbing atom is in a molecule or structure, the region above the absorption edge will not be smooth, but have a sinusoidal shape. These are the oscillatory variations in the absorption spectrum referred to as EXAFS, and they last until about 1000 eV above the edge. This *fine structure* of the spectrum is due to the sum of interferences between the outgoing and all the backscattered waves. The frequency and amplitude of the sinusoidal variations in the absorption rate depends on the distances of the neighbours to the absorber, and the type (and bonding) of neighbours, respectively [18; 19]. An example of an absorption spectrum is shown in fig. 5.

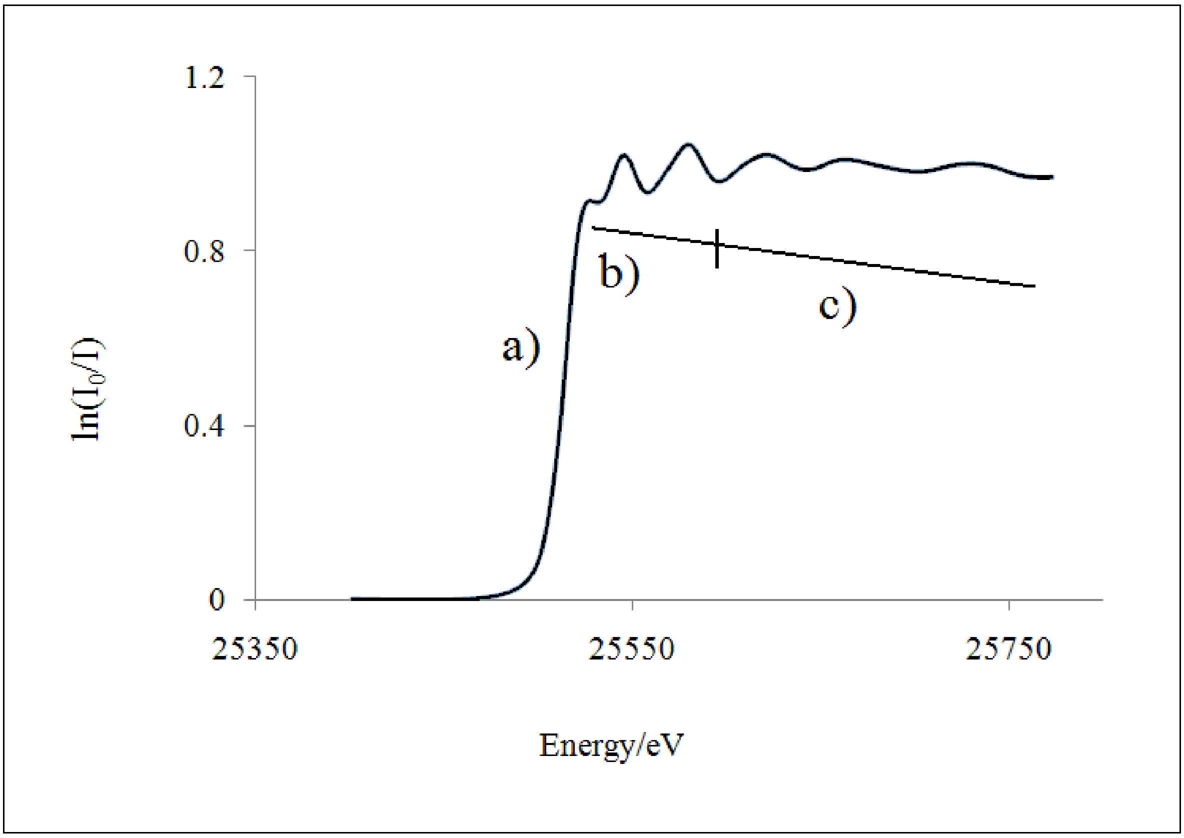

Figure 5: *An example of a XAS-spectrum. This is the absorption spectrum of silver(0) foil, where a) is the K-edge (25514 eV for silver), b) is the XANES region of the spectrum, and c) is the EXAFS region.*

The EXAFS is generally in the region 40 to 1000 eV above the edge, and the X-ray Absorption Near Edge Structure (XANES) is approximately from 20 eV before the edge to 50 eV above [18]. The XANES can give information about electronic configuration, valence state, site symmetry and coordination number of the absorbing atom. The energy of the edge is moved to a higher energy (1-3 eV) when increasing the valence state of the absorber, because decreasing the number of valence electrons increases the effective nuclear charge, and thus the ionization energy [18].

The photoelectron ejected from the absorbing atom will move like a spherical wave with the wavelength $\lambda = {}^{2\pi}\!/_{k}$, where k is the wave vector of the photoelectron, defined by

$$k = \sqrt{\frac{2m}{\hbar^2}(E - E_0)} \tag{4}$$

where $\hbar = h/2\pi$, E is the energy of the incident photon and E_0 is the threshold energy of the edge, $(E-E_0)$ is the kinetic energy of the photoelectron and m is the mass of the electron. At moderate thermal or static disorders and high energies above the edge (≥ 60 eV), the modulation of the absorption rate in EXAFS is given by

$$\chi(E) = \frac{\mu(E) - \mu_0(E)}{\mu_0(E)} \qquad (5)$$

here normalized to the background absorptions (μ_0). $\mu(E)$ is the measured absorption at a given energy, and $\mu_0(E)$ is the curve that would have been observed if the absorber was an isolated atom. This is a factor that cannot be measured, as it is impossible to isolate atoms, with the exception of monoatomic gases. For this reason, the value of $\mu_0(E)$ is estimated when procedures of removing background is performed, by determining a smooth curve following the path of the EXAFS [18; 19].

With the purpose of relating $\chi(E)$ to structural parameters, it is necessary to translate the energy *E* to the wave vector *k* of the photoelectron. This conversion from *E*-space (eV) to *k*-space (Å^{-1}) is performed with eq. 4, and gives rise to the EXAFS equation, $\chi(k)$:

$$\chi(k) = \sum_j N_j S_i(k) F_j(k) e^{-2\sigma_j^2 k^2} e^{-2r_j/\lambda_j(k)} \frac{\sin(2kr_j + \phi_{ij}(k))}{kr_j^2} \qquad (6)$$

The N_j is the number of neighbouring atoms of type *j*, the $F_j(k)$ is the backscattering amplitude for each of the N_j atoms with a Debye-Waller factor σ_j, and at a distance r_j from the absorbing atom. $S_i(k)$ is a factor of amplitude reduction from many-body effects like shake up/off-processes at the absorbing atom *i*. The λ_j is the mean free path of the electrons, and the expression $e^{-2r_j/\lambda_j(k)}$ is owing to inelastic losses in the scattering or due to the medium in between. The total phase shift experienced by the photoelectron is $\phi_{ij}(k)$ [18; 19].

The amplitude of the signal from a neighbour is radically reduced as the distance from the absorber increase ($1/r^2$), thus EXAFS can only give information about the closest coordination shells (~1-5Å). The amplitude function $F_j(k)$ depends only on the type of backscatterer, because the photoelectron is scattered by the core electrons of the neighbour. Thus, the amplitude gives information about the type of neighbours in the different shells. It should be mentioned though, that EXAFS cannot distinguish between elements next to each other in the Periodic Table [18; 19].

There are two terms in the EXAFS equation that contribute to reduction in the amplitude. $S_i(k)$ depends only on the absorber, and represent multiple excitation of the absorber. Not all the energy of the X-rays hitting the atom leads to excitation of the 1s electron to the continuum. Some of the energy of the photoelectron can transfer to other electrons in the absorber and lead to shake-up (excitation of electrons to higher energies) or shake-off (excitation of electrons to continuum) processes. This gives the emitted photoelectron a lower kinetic energy than $(E-E_0)$. The second term that contribute to reduction in the amplitude is the inelastic scattering, expressed by $e^{-2r_j/\lambda_j(k)}$. This expression is related to the lifetime of the excited state of the absorber. The expression signifies the probability of the photoelectron to travel from the absorber to the neighbour and back, without inelastic scattering or the core hole being filled. When this occur an EXAFS signal will be obtained [18].

The Debye-Waller factor σ is defined as the root mean square displacement of the average nearest neighbour distance [19]. It contains important chemical and structural information, and plays an important role in EXAFS spectroscopy. σ corresponds to variations in the interatomic distances due to thermal vibrations of the atoms and static disorders [18; 19].

The photoelectron experiences phase shifts as it moves from the absorber to the neighbour and back. The total phase of the backscattered wave, $\sin(2kr_j + \phi_{ij}(k))$, can be considered in two parts. First is the distance the photoelectron travels, $2r_j$ (from the absorber to the backscatterer and back). This distance corresponds to a number of wavelengths $2r_j/\lambda_e$, where λ_e is the wavelength of the photoelectron (see fig. 3). This gives a phase change given by $(2\pi \times 2r_j/\lambda_j)$ which in turn gives $2kr_j$ $(k = 2\pi/\lambda_j)$. The second part of the phase expression is $\phi_{ij}(k)$, which is a sum of $2\times$ the interaction with the potential of the absorber (one time going out, and one time coming back) and $1\times$ the interaction with the potential of the backscatterer. This part of the phase expression describes only 10% of the total phase, however it is still important to consider it to be able to find the binding distance to the neighbours within ±0.02 Å of uncertainty. Thus, it is required that these phase parameters are known, to determine the interatomic distances [18; 19].

2.3.2 Experimental setup

The transmission experiments performed in this thesis were carried out at the Swiss-Norwegian Beamlines (SNBL) at the European Synchrotron Radiation Facility (ESRF), which is a third generation synchrotron. A synchrotron source provides a flux of the photons that is twelve orders of magnitude more intense than usual X-ray sources. This is required to attain a high signal-to noise spectrum within 30-40 minutes, as opposed to days of recording with conventional X-ray sources.

The experimental stations are usually placed at the output on one of the bending magnets, as the photons produced there have a high and uniform flux over a large energy range. The SNBL-beamline provides X-rays in the energy range 4 to 70 keV [20].The polychromatic beam of white light is sent through a monochromator which focuses the beam to monochromatic X-rays of a chosen energy. The monochromator at the SNBL is a channel-cut Si[111] crystal monochromator, where the wavelength is chosen according to Bragg's law, and the energy is changed in a stepwise manner by movement of the crystal. The monochromatic X-rays are then sent to the hutch via two focusing mirrors covered with Cr and Au, which rejects the higher harmonics of the beam (glitches). The spot size of the beam is up to 10 X 0.6 mm [20]. A sketch of the experimental setup for a transmission experiment is outlined in fig. 7.

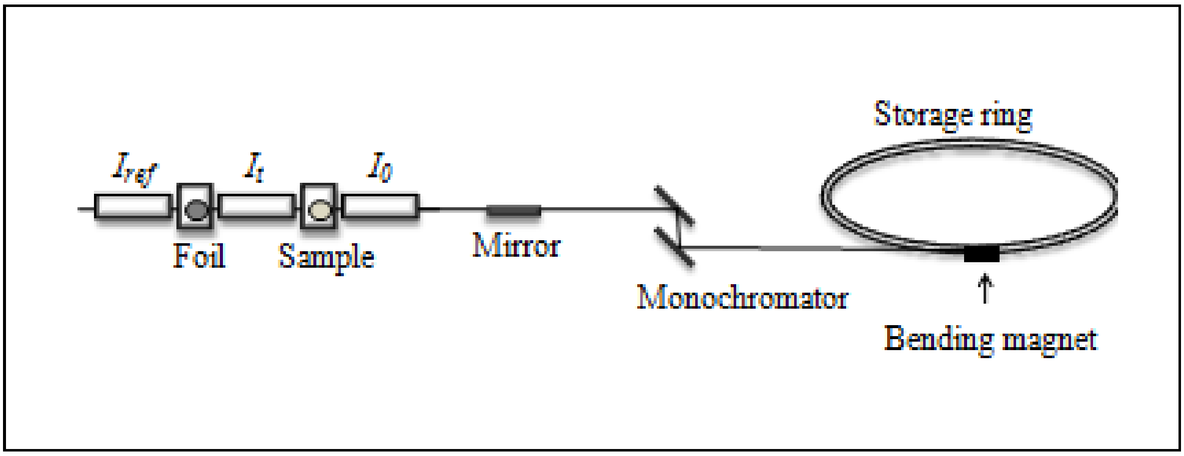

Figure 7: *The experimental setup for a transmission XAS experiment.*

The focused, monochromatic beam is sent to the experimental station (hutch) where it first passes through an ion chamber to detect the incident intensity (I_0), and then it passes through the sample. The beam is thereafter passed through a second ion chamber to detect the transmitted intensity (I_t), in order to measure the absorption of the sample as a function of photon energy. At last, a third ionization chamber measures the absorption of the reference foil (bulk metal of the element being investigated). The ion chambers are filled with either one inert gas, or a mixture of inert gases. When X-rays pass through the ion chambers, the gases are ionized and thus give off an electric signal which can be correlated to the intensity. The gases are chosen according to the energy of the beam, and account for 20% (I_0) and 80% (I_t) of the absorption. Instead of ionisation chambers, the intensity of the photons can also be measured by means of scintillation counters or solid state detectors.

If the element being investigated is present in very small amounts, it can be preferable to use fluorescence mode instead of transmission mode. This technique will increase the signal to noise ratio, because it removes the background absorption (due to other constituents), and thus improve the sensitivity. The sample is placed at a 45° angle to the incident beam, and the fluorescent radiation (secondary radiation as the core hole relaxes) is measured by a 13 element Ge detector with fast digital multi channel analyzer electronics [20]. The signal is amplified and converted in the same way as in transmission experiments.

2.3.3 Data analysis

The extraction of structural information from a XAS spectrum is a procedure which consists of several steps concerning substantial data processing. The EXAFS and XANES data in this thesis has been treated using the `Athena` software from Ifeffit. Thereafter the `EXCURV98` software was used to refine the EXAFS and extract structural parameters. In `Athena` there has been performed

- ✓Conversion of raw data into $\mu(E)$
- ✓Summing of multiple scans of a sample
- ✓Energy correction against the foil
- ✓Choosing E_0
- ✓Deglitching and truncation
- ✓Pre-and post-edge fitting to normalize the spectrum
- ✓Background removal
- ✓Conversion from $\mu(E)$ to $\chi(k)$
- ✓Linear combination fit of XANES

First the raw data were read into `Athena`, and multiple scans of the same sample were summed to increase the signal-to-noise ratio. Then the energy was corrected (calibrated) against the foil value, and E_0 selected by choosing the first peak of the first derivative of $\mu(E)$ [21].

The spectrum may contain some false points called glitches, due to the monochromator, electronics or the sample itself. These glitches must be removed, because they can alter the background removal. Also, the spectrum can be truncated if there is much noise, and this can be performed both in the pre-edge region and the post-edge region. However, these operations should be done with great care, because if one truncates or deglitches too much, important information may be lost in the process [21].

Normalization is a process of regulating the data with respect to aspects of the measurement, such as preparation or sample thickness. When data are normalized, they can be directly compared, without any regard of the experimental details. Normalization is also necessary for XANES comparison with model samples. When normalization is performed, a line is regressed to the data in the pre-edge range, and a polynomial is regressed to the data in the post-edge range. The regressed line in the pre-edge range is extrapolated to all the energies in the measurement range, and subtracted from the spectrum, and thus the absorption background is removed from the whole spectrum. The post-edge regression is called the normalization range, and is performed in order to make the jump (K-edge) of the spectrum to go from 0 to 1 in absorption (μ, see eq. 3), regardless of the thickness of the sample. In this way, the XANES spectra to be compared have the same absorption jump, if their normalization range is the same. `Athena` calculates and removes the background, but the post-edge regression can affect the background to some extent. The data prepared for EXAFS analysis in `Athena` do not have to be normalized in the same manner, but it is important to control that the slope of the calculated the background ($\mu_0(E)$) follow the slope of the absorption spectrum, and do not oscillate. It is of high importance to have a proper background removal to attain successful EXAFS refinements [21].

It is possible to estimate the quantities of the species in a sample. This is performed by a linear combination of standard spectra to the unknown spectrum. These fits can be carried out in $\mu(E)$ or $\chi(k)$, and it is important that the spectra being compared are normalized in the same range, e. g. -30 to 150 eV. The mathematical formula used in `Athena` to evaluate the quality of the fit is

$$\frac{\sum (data - fit)^2}{\sum (data)^2} \tag{7}$$

where the sums are over the data points in the fitting region, usually from -20 to 60 eV [21].

When the background was removed and the energy corrected, data were treated in `EXCURV98`, where a calculated model ($\chi_{th}(k)$) is least square fitted to the experimental spectrum ($\chi_{exp}(k)$). The EXAFS equation (eq. 6) generates $\chi_{th}(k)$, and by fitting this theoretical model to the experimental $\chi_{exp}(k)$, refined structural parameters can be extracted. In order to find reliable values of the parameters to be refined (Debye-Waller factor ($2\sigma^2$), multiplicity (N) and interatomic distances (r)), the other parameters need to be known. Phase shifts ($\phi_{ij}(k)$), backscattering amplitudes (F_j) and inelastic scattering losses ($e^{-2r_j/\lambda_j(k)}$) are calculated by the program itself, using the Hedin-Lundquist method. The amplitude reduction factor ($S_i(k)$) is called AFAC in `EXCURV98`, and is determined using a model compound with known structure. The total amplitude is dependent on AFAC, N and $2\sigma^2$, which are all correlated, thus they cannot be refined all at the same time. AFAC is determined for the model compounds by setting N constant (known), and is subsequently transferred to the unknown samples. It is important that the models resemble the structure of the unknown samples, in order for it to be transferable. Thus, the foil is used as a model when the unknown sample is assumed to be in oxidation state 0 (metallic) and oxides are usually used for other oxidation states of the element being investigated [18; 19].

The EXAFS amplitude is dampened at high *k*-values, and to compensate for this, the $\chi(k)$ is weighted by a power of k; $k^n\chi(k)$, where n= 1, 2, 3. Neglecting this weighting may affect the interatomic distances because oscillations with larger amplitudes will dominate over smaller amplitudes. How the chi-curve should be weighted is dependent on the atomic number (Z) of the neighbours, and the recommended weighting is n=1 for Z>57, n=2 for 57<Z<36 and n=3 for Z<36. A k^3-weighting will minimize the chemical effects on the EXAFS signal, which is most significant at lower *k*-values. In addition, the k^3-weighting will compensate for the $1/k$ part of the EXAFS equation, and also the $1/k^2$ dependence of the back scattering function ($F_j(k)$ is nearly proportional to $1/k^2$ at high *k*-values in the Born approximation). However, it is important to weight all samples by the same order to be able to compare them, and it is especially important to have the same weighting for the models and the samples for the AFAC to be transferable [18].

An indication of the quality of the fit between the experimental and theoretical EXAFS spectrum can be obtained from the *R*-factor, which is defined by

$$R = \sum_i^N [1/\sigma_i (| \chi_i^{\exp}(k) - \chi_i^{th}(k) |)] \times 100\% \tag{8}$$

An *R*-factor around 20% is considered a reasonable fit [22].

Fourier Transformation (FT) is a way of separating the different sinusoidal waves that together make the EXAFS signal. The procedure converts each frequency in the signal into a separate peak in the FT-spectrum in *r*-space. Each peak represents one specific shell of neighbours, and the centre of the Gaussian distributed peak corresponds to the distance between the central atom and the atoms in the shell. The Fourier Transformed EXAFS signal provides qualitative structural information about the surrounding environment of the absorber. The positions of the FT-peaks depend on the phase parameters, and the heights depend on amplitude parameters. Also the weighting of the chi-curve will influence the peak heights and positions [18].

The k-range of the chi-curve influences the resolution of the FT-curve, and as a result, a small k-range can give total or partial overlapping of the peaks in the FT-curve. The peaks in the r-space are shifted 0.2-0.5 Å from the true value, depending on i.a. the elements, the E_0 chosen in `Athena`, and the weighting of the chi-curve. These shifts can be obtained from model compounds which have known values, and the shifts can be transferred to the unknown system. However, it is provided that the models and the unknown samples have been treated in the same manner, and that they possess similar environment in the structures, e.g. oxidation state of the absorber [18].

To determine the type of neighbouring atoms, it is possible to isolate one of the peaks in the FT-curve, and subsequently back transform the signal into *k*-space. It is now possible to refine this signal, which is a result of only one of the shells, and discover which kind of element that gives the best *R*-factor. The element with the lowest *R*-factor is the most likely neighbouring element. This procedure is called Fourier Filtering, and it can be useful when in doubt about the backscatterers. However, as mentioned earlier, it is not possible to distinguish between elements that are next to each other in the Periodic Table, because they have too similar atomic weight [18; 19].

The multiplicity found in a data refinement of EXAFS can be used to determine the size of metal clusters in a sample. deGraaf et al. used eq. 7 to calculate the size of the Pt clusters in their samples.

$$N_{Pt-Pt} = \frac{MW_{Pt}}{N_{Av} \times Pt_{loading}} \int_{size=0}^{\infty} P / g_{zeolite}(size) \times A(size) \times N_{Pt-Pt}(size) d(size) \qquad (9)$$

where MW_{Pt-Pt} is the molecular wight of platinum, N_{Av} is Avogadro’s number, $Pt_{loading}$ is weight of platinum per weight of zeolite, $P/g_{zeolite}(size)$ is the number of particles per size per gram catalyst (complete particle size distribution), $A(size)$ is number of platinum atoms per particle size, and $N_{Pt-Pt}(size)$ is the first shell coordination number of platinum particles per size [23]. This equation gave the plotted graph in fig. 6.

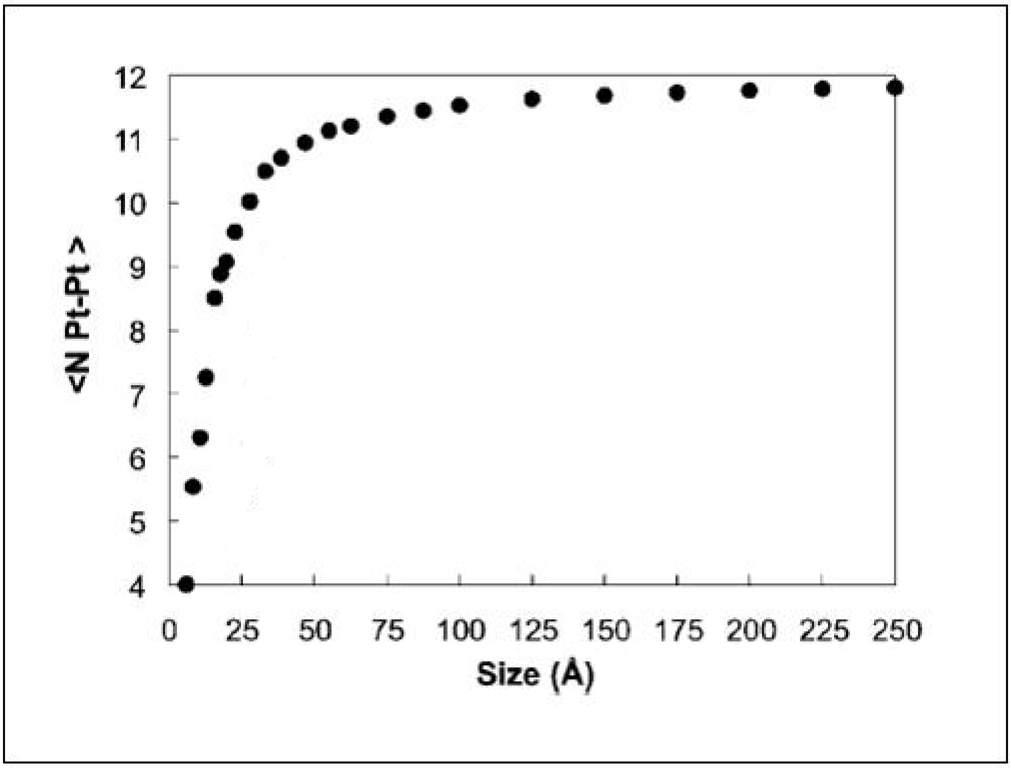

Figure 6: *The plot from deGraaf et al. using eq. 7. [23]*

The plot in fig. 6 can be used to estimate the cluster size of other metals (Me), when $P/g_{zeolite}(size)$ and $A(size)$ are unknown. This is done by correcting for the difference in binding distances between Me and Pt, and multiplying this relationship with the multiplicity from the EXAFS refinement of the metal in question. For example, to find the size of a silver cluster with a multiplicity of 9.2, it is necessary to multiply it with the factor r_{Ag}/r_{Pt} (2.889/2.776 = 1.040706052), which gives a relative multiplicity of 9.57. This relative multiplicity can be read off the graph in fig. 6 to directly find the size of the silver cluster. It must be mentioned that this is performed manually, which gives relatively large uncertainty. However it is a useful way to obtain an indication of the size of the clusters.

When the size of the cluster is known, one can calculate how many atoms the cluster contains. This is performed with eq. 8 [15]:

$$N = 4\left(\frac{\pi}{6}\right)\left(\frac{d^3}{a_0^3}\right) \tag{10}$$

where N is the number of atoms, d is the diameter of the spherical clusters and a_0 is the lattice constant (a_0 = 4.1 Å for silver bulk metal) [15]. Example: The maximum number of silver atoms that can fit into the 7.4 Å pores of an APO_4-5 is 11.8 atoms.

These calculations are useful to determine whether the clusters investigated are inside the pores of the microporous carrier, or if they are too big, and thus has to be on the surface. However, as mentioned, there are large uncertainties involved, and this must be kept in mind when considering these results to draw conclusions.

2.3.4 Advantages and limitations of EXAFS

As with every other experimental technique, there are both advantages and limitations to the use of EXAFS. It is a very sensitive analytical tool, able to detect elements at ppm level [18]. The principal advantage of EXAFS is the opportunity to probe local structure. Long-range order is not required, and there are no limitations to the physical form of the sample being studied. The technique is therefore used to study a variety of materials, including biological and amorphous materials. These systems are non-crystalline, thus structural information is not easily obtained by other techniques, such as conventional XRD, which require a long range crystalline structure. A disadvantage is the limitation of the distance; EXAFS can only provide information about the structural environment up to ~5 Å from the absorbing atom, thus no long range order or structural trends can be determined. In addition, the method is a bulk technique sensitive to all the forms of the element being investigated. Hence, if the element of interest is in a mixed environment, only the average structure is determined [24]. As previously mentioned, it is possible to estimate metal cluster sizes with the coordination number obtained from EXAFS refinements. However, the values obtained are average for all the clusters present, thus no size distribution can be found.

2.4 Additional methods

In addition to XAS, several methods have been used in this thesis to characterise the samples and their properties. This chapter will give a short introduction to the principles of these the methods.

2.4.1 X-ray Diffraction

Diffraction is a well known phenomenon in physics, and in the case of X-ray diffraction the waves of the X-rays will interfere when an object is in their pathway, and this interference can be used to analyze the object in their path. When the X-rays have a wavelength of about 0.1 nm, they will be scattered by electrons in the atoms, and diffraction will occur if the atoms have a long range structure (e.g. crystals) with binding distances in same range as the X-rays. A way to explain the physics in X-ray diffraction is to picture the layers of atoms as parallel planes with a distance d, see fig. 8. The X-rays will be reflected from these planes (the planes will typically be referred to with their Miller indexes ($h\ k\ l$), but this will not be further elaborated in this thesis), and the constructive interference of the waves (λ) will occur when the incident angle, θ is defined as

$$2d \sin\theta = n\lambda \tag{11}$$

where n is an integer. This relationship is called the Bragg equation, and it gives an opportunity to investigate the structure when the diffraction angles and intensities are measured [25].

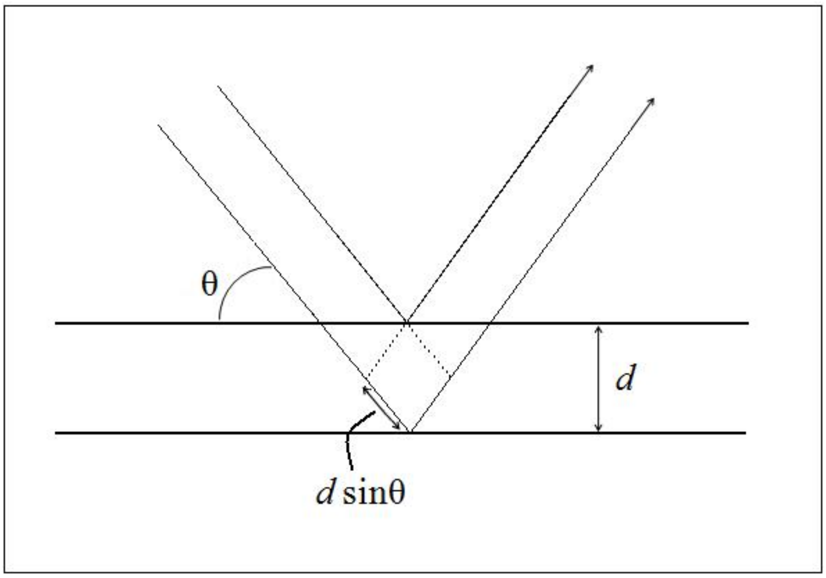

Figure 8: *Reflection of two parallel X-rays which leads to constructive interference if the 2dsinθ is equal to an integer multiple of the wavelength.*

There are two types of XRD; powder X-ray diffraction and single-crystal X-ray diffraction. In single-crystal diffraction, a large single crystal (>tens of micrometers) is investigated; however this is not always uncomplicated. Single crystals are usually not easily made, and not every compound can be grown into a single crystal. Thus powder X-ray diffraction is typically the most applicable method. The polycrystalline powder consists of thousands of crystallites (0.1-10 µm) with random orientations. When the X-rays hits the powder sample, the scattered waves goes out in all different directions. Every plane in the crystal with different spacing will result in a different cone of diffraction intensity. Each cone is made from many small close dots which each represent one of the crystallites. To determine all possible cones of diffraction, the detection of the diffracted X-rays is performed around the whole circumference of the sample. In this way, the intensities are recorded as a function of the detection angle, 2θ/°. The peak intensities in the diffractograms are dependent on the type of atom, and where this atom is placed in the unit cell. The position of the peaks and the number of peaks are dependent on the crystal system, cell parameters, lattice type and wavelength used to collect the data [25].

X-ray diffraction is very useful for fingerprinting of crystalline solid, since about all crystal systems have a unique X-ray diffraction pattern, as regards peak positions and intensities. Many of these unique and known data sets are collected into a data base by the Joint Committee on Powder Diffraction Standards (JCPDS). The data base contains more than 50 000 powder diffraction patterns and it is used as a fingerprint library. This makes it possible to identify unknown samples, or confirm the presence of a product from syntheses etc. [25].

2.4.2 Inductively Coupled Plasma Mass Spectrometry

Inductively coupled plasma mass spectrometry (ICP-MS) is a widely used technique for analyzing the elements in a sample. The technology with the inductively coupled plasma came in the 1970s, and led mass spectrometry into a new era. The method can determine more than 70 elements within a few minutes, with accuracy down to the ppt level [26].

To analyze the elements in a sample, the solid matter usually has to be solved in an aqueous solution, in order to inject them into the plasma via a nebulizer. The elements are ionized by the inductively coupled plasma, and the ions are sent into a mass spectrometer for analysis. The mass spectrometer separates the elements by mass-to-charge ratio (*m/z*), and there are different technologies used to perform the analysis. A high resolution ICP-MS usually consist of a magnetic sector with double focusing. The ions from the plasma (atmospheric pressure) are transported into the mass analyzer (high vacuum) through a metal cone with a small orifice. First, the ions are sent through an electrostatic field which focuses the beam of ions into a slit leading to the magnetic sector. The magnetic sector will separate the ions based on their deflection in the magnetic field, and the curve of the ions depend on their *m/z* value. The magnetic sector is scanned to bring elements of different *m/z* values to a detector [26].

The resolution of a mass analyzer is defined as

$$R = {}^{m}\!/_{\Delta m} \tag{12}$$

where m is the nominal mass at which the peak occurs, and Δm is the width of the peak. This means that a higher R gives a better resolution, and a typical high resolution ICP-MS has resolutions up to 10 000. This high resolution ICP-MS equipment is very expensive; however they achieve excellent detection limits [26].

2.4.3 Transmission Electron Microscopy

The principle behind transmission electron microscopy (TEM) is electrons passing through a sample, and thus interacting with the matter. An image is created by the exiting electrons when they illuminate a fluorescent plate, or are detected to be viewed as an image on a conventional screen. The human eye cannot see electrons, thus the electron image need to be converted to visible light. The best TEM’s today have a resolution down to the single Ångstoms range, in contrast to an optical microscope device having a resolution of 2000 Å, at best [27].

The TEM consists of three major fractions; the source of electrons, the image producing system and the image recording system. The electrons come from a shielded, pointed electron gun which is heated, which can be made of tungsten or a single crystal of lanthanum hexaboride (LaB_6). This serves as a cathode, and has a negative potential equal to the chosen accelerating voltage. After the cathode, there is a disc formed anode with an axial hole. The electrons will accelerate from the cathode through the anode at a constant energy related to the effective wavelength of the electrons, which establish the “optical” quality of the TEM. A condenser system concentrates the beam of electrons onto the sample; typically the instrument has two of these condenser lenses, to control the size of the illuminated area on the sample [27].

In the image producing system the exiting electrons are first sent through a objective lens which produces a real image of 20-200 magnification. This image is further magnified by two projector lenses. The final magnification can range from 1000 to 250 000. In the early days of the TEM technology, the image recording system consisted of a fluorescent plate placed at the end of the microscope to convert the electrons into visible light, or a photographic emulsion to make a image negative. Today a conventional television screen presents the final image [27].

When one increases the accelerating voltage, the effective wavelength will be smaller and the resolution will be higher. TEM’s with an accelerating voltage of over a million volts have been created, which gave a resolution of ~0.7 Å. However, these devices were extremely expensive. Now, more commercially friendly TEM’s have been made with new and improved technology, allowing lower voltage (~200 kV) to achieve resolutions of ~2 Å [27].

TEM is applicable in many disciplines, and is frequently used in biology and medicine, among others. In medicine the TEM can be used for diagnostic purposes, and in biological research direct observations of cell walls and cell nuclei have been made possible [27].

2.4.4 Scanning Electron Microscopy

As electrons are a form of ionization beams, their interaction with matter will create a wide range of secondary signals from the sample. The electrons can either be backscattered, produce secondary electrons from core electrons of the atoms on the sample, create Auger electrons, visible light, characteristic X-rays, elastically and inelastically scattered electrons, and Bremstrahlung X-rays. All of these signals can give information about the sample if they are detected and treated right. Scanning electron microscopy (SEM) is based on these secondary signals reflecting back from the sample, and not the electrons passing through the sample as in the TEM technology. SEM provides images in 3D, and TEM provide images in 2D. The device consists of an electron source, a lens system and an electron collector [27].

The source of the electrons is, as in TEM, an electron gun made of a tungsten or lanthanum hexaboride cathode which is heated. The electron gun provides a small electron beam with a large stable current. The lens system (usually 1-3 lenses) is used to decrease the size of the beam, and is called a crossover. The crossover diameter may be 10-50 µm which gives a spot size of 1 nm to 1 µm that hits the sample. The final electron beam diameter (spot size) limits the resolution in the SEM, and the intensity of the emitted signals depends on the current in the final probe [27].

The recording of the images take place in a closed system which is kept in vacuum in the operational state [28]. The SEM records the secondary signals released from the sample, which gives a 3D image of the sample. The detector has to convert the collected signals into a useful signal, and the secondary signals that usually are collected from the sample are secondary electrons (SE)[3] and backscattered electrons (BSE)[4]. The secondary electrons have low energy and come from only a few atomic layers beneath the surface of the sample. The backscattered electrons have higher energy and can escape from several nanometres into the surface of the matter. The backscattered electron can carry information about the chemistry of the sample, such as average atomic number, but they are not produced in a large amount. In contrast, the secondary electrons are produced in large quantities, and are easily collected. The detector creates a signal from both secondary and backscattered electrons, and the SEM images can be chosen to be recorded in either BSE mode or SE mode [27].

---

[3] Secondary electrons are emitted from the atoms in the sample, given a small amount of kinetic energy by inelastic collisions with electrons from the beam.

[4] Backscattered electrons from the beam backscattered by the sample as a result of multiple elastic scattering.

Any object can be investigated by a SEM, as long as it is electrically conductive. If the sample is insulating, it is usually coated with a thin layer of gold or carbon to make it electrically conducting. The contrast formed by the collected signals is due to the difference in surface topography and composition, whereas SE images are dominated by topological contrast and BSE images are more oriented to detecting atomic density [28].

The SEM images recorded in BSE mode are often not very sharp and not easy to interpret, but they can provide a mapping of the different elements in a sample. The images recorded in SE mode are often sharper and easier to interpret as regards shape of the particles in the sample [27].

2.4.5 Thermogravimetric Analysis

Thermal analysis can be conducted to investigate how a sample responds to heat. The sample is heated and the mass is measured as a function of temperature. The apparatus used to collect these data is called a thermobalance and consist of a temperature programmable furnace, an electronic microbalance and a controller. The thermobalance allows the sample to be heated and weighed at the same time. The heating programme can be adjusted to be linear, isothermal heating, or more complex heating and cooling schemes. The heating takes place in a closed system to be able to control the atmosphere of the heating. It is possible to carry out the experiment in an inert atmosphere, in air or whatever the investigation requires. It is also possible to choose static or flowing atmosphere. If flowing atmosphere is chosen, the possibly evolving volatile or corrosive gases may be evacuated, thus preventing condensing of gases from the reaction. The gases can be fed to a mass spectrometer to detect and identify the species, which can be useful when trying to understand what happens when the sample loose or gain weight. TGA is most useful for investigating dehydration, decomposition, desorption and oxidation processes [25].

The mass spectrometer identifies the species in the exhaust by measuring the mass-to-charge ratio, in the same manner as the ICP-MS, but in a much less complicated way. In a TGA analysis the mass of the compounds coming out are detected, not the elements [25], so that the mass of N_2 (28.01345 amu) is not easily distinguished from the mass of CO (28.0103).

When the sample is heated and the species going off is detected, the thermal events can also be detected. This can be performed by differential scanning calorimetry (DSC), where the sample and a reference are kept at the same temperature during the heating procedure. The heating of the two takes place with different power supplies, and if a thermal event appears, this will be registered as a difference in power supply. As an exothermic event happens in the sample the power supply needed to keep the temperature will be smaller, and vice versa for endothermic events [25].

2.4.6 The Brunauer–Emmett–Teller method

In order to measure the surface area of a porous sample, the Brunauer-Emmett-Teller method (BET) is frequently used. This is a gas sorption technique, and is based on physical adsorption of gases to a surface. The molecules of the adsorbing gas (sorbate) are free to cover the whole surface, and thus the determination of the surface area is possible. The BET method is named after its inventors, and the theory is based on a few assumptions: All sorption sites are energetically similar, the heat of adsorption of the first adsorption layer is constant and the heat of adsorption of the second and subsequent layers are equal to the heat of liquefaction. BET is a multilayer theory, in contrast to Langmuir’s approach with monolayers. The complex mathematical theory will not be described thoroughly here, but it is based on the assumptions mentioned above, in addition to the kinetic equilibrium between the gas and the adsorbed molecules by means of pressure. By plotting the amount of gas adsorbed at a surface against the relative pressure (called a sorption isotherm), it is possible to estimate the amount of gas needed to form a monolayer, and thus the surface area can be determined. Several gases can be used to measure the surface of a sample, but nitrogen is the most frequently used. The BET method is useful for solids with pore diameters above ~4 nm; below this the calculations are believed to be inaccurate [28].

Experimental

3.1 *The synthesis*

The syntheses of $AgAPO_4$-5's were carried out by modifying the recipe of Muñoz et al. (1998) [29]. Different silver sources were added to the synthesis gel, and also different templates were used. The silver sources used in this thesis are silver(I) oxide, silver(I) acetate, silver(I) sulphate and silver(I) nitrate. The templates used in the syntheses of $AgAPO_4$-5' were triethylamine (TEA) and methyl dicyclohexylamine (MDCHA). In the synthesis of the AgSAPO-11, the recipe of Lee et al. (1991) was modified, and i-diisopropylamine (i-Pr_2NH) was used as the template [30].

In a typical synthesis of $AgAPO_4$-5, the hydrogel was made by first mixing orthophosphoric acid (13.6 g, H_3PO_4, 85%, Merck), deionised water (18.02 g) and silver sulphate (Ag_2SO_4, 0.3 g, Merck). This was stirred until the silver salt had become completely dissolved. Subsequently pseudobohemite was added (7.1 g, ALOOH, Sasol North America Inc.), and the slurry was stirred until it was homogenous. Finally the template MDCHA (20.1 g, Sigma-Aldrich) was added. The final white hydrogel was either set to ageing for 24 hours before crytallization, or poured directly into stainless steel autoclaves lined with Teflon, to be crystallized for 24 hours at 150°C. pH was measured before the crystallization, usually around 7.

After crystallization, the product was filtered and washed with approximately 500mL of deionised water. The product was dried in air at 100°C for 24 hours, and calcined at 550°C in air for 17 hours, with the temperature increasing and decreasing with 1°C/min. The products were brown before calcining, and white after calcining.

In the synthesis of AgSAPO-11, orthophosphoric acid (15.5 g, H_3PO_4, 85%, Merck), deionised water (40 g) and silver nitrate ($AgNO_3$, 1.38 g, VWR^{TM} Prolabo) was mixed. Subsequently finely ground aluminium isopropoxide was added (27.2 g, Al(O-i-Pr)$_3$, Sigma-Aldrich). After one hour of stirring, SiO_2 was added (3.73 g, 40 wt% suspension, Sigma Aldrich) with deionised water (3.6 g). Finally the template i-Pr_2NH (6.34 g, Sigma Aldrich) and water (4 g) was added drop by drop. The final white hydrogel was set to ageing for 24 hours. pH=11 was measured before the crystallization. The final gel was poured into stainless steel autoclaves lined with Teflon, to be crystallized for 24 hours at 200°C. The product was washed, dried and calcined in the same manner as the APO_4-5 samples. The as-synthesised product was yellow-brown, and the calcined product was light brown.

It was made an attempt to find out when the silver is autoreduced in the autoclave (indicated by the brown colour), and whether this happens before or after the crystallization of the APO_4-5. A large amount of hydrogel was made in the same way as the typical synthesis of $AgAPO_4$-5, just multiplying the recipe with 3. The silver source was silver acetate and the template was MDCHA. Four autoclaves was put in an oven at 150°C, and was taken out one by one after 1 hour, 2 hours, 3 hours and 4 hours. The sample taken out after one hour was light grey-brown, and the colour became darker in the samples after 2, 3 and 4 hours. The products were washed, dried and calcined in the same manner as the earlier samples.

In addition, several samples of AgAPO-5, AgSAPO-5 and AgAPO-11 with different combinations of templates and silver sources were attempted made at a crystallization temperature of 100°C for 24 h. The products had all different types of colours; pink, purple, yellow, brown and black.

As all the typically synthesised samples became brown, (except $AgAPO_4$-5/3, which was yellow), indicating silver metal, ion exchanged samples were prepared to be able to study cluster formation with *in-situ* EXAFS. The parent SAPO-5 and SAPO-11 were synthesised by modifying the method described by Lok et al. (1984) [31]. The selected amount of pseudobohemite (AlOOH, Sasol North America Inc.) was dissolved in a mixture of orthophosphoric acid (H_3PO_4, 85%, Merck) and water. The solution was stirred for 30 minutes until the slurry was homogenous, before adding the silicon source (AS-40, 40 wt% SiO_2). Finally the templates triethylamine (TEA, 99% Aldrich) for SAPO-5 and n-dipropylamine (n-DPA, 98%, Aldrich) for SAPO-11 were added to the homogenous gels and the mixtures left under stirring for two hours. The final gels were poured into stainless steel autoclaves lined with Teflon to be crystallized at 200 °C for 48 hours. The crystalline products obtained was washed, dried and calcined in the same manner as the APO_4-5 samples.

The calcined SAPO-5 and SAPO-11 parent materials (2 g) were ion exchanged with a solution of $AgNO_3$ (60 mL, 0.1 M). The mixture was stirred for approximately 24 hours, before washing with deionised water, drying at 100°C and finally calcining in the same manner as the hydrothermally synthesised samples.

The silver sources and templates used in the different syntheses and ion exchange procedures are given in table 1.

Table 1: *Ingredients and molar composition of the samples used hereafter. Two samples were ion-exchanged, indicated by a colon (:).*

Sample	**Ag source**	**Template**	**Ag:Al ratio**	**Molar composition Al: P: Si: H_2O:Template**
$AgAPO_4$-5/1	AgAc	TEA	0.05	1 : 1 : 0 : 16.8 : 1.5
$AgAPO_4$-5/2	Ag_2O	TEA	0.08	1 : 1 : 0 : 16.8 : 1.5
$AgAPO_4$-5/3	Ag_2O	MDCHA	0.08	1 : 1 : 0 : 11: 1
$AgAPO_4$-5/4	Ag_2SO_4	MDCHA	0.0260	0.43 : 1 : 0 : 8 : 0.5
AgSAPO-11	$AgNO_3$	i-Pr_2-NH	0.06	1 : 1 : 0.17 : 20 : 0.47
Ag:SAPO-5	$AgNO_{3\,(aq)}$	TEA		1 : 1 : 0.2 : 30 : 0.6
Ag:SAPO-11	$AgNO_{3\,(aq)}$	n-DPA		1 : 1 : 0.2 : 20 : 0.5

All of the syntheses and ion exchange procedures were carried out with no direct light at the gel and product. It was attempted to cover the containers as much as possible with aluminium foil, to keep the syntheses in the dark, as silver(I) reacts with light to be reduced to silver(0).

3.2 XRD

X-ray diffraction data were collected at NTNU using a Siemens D5005 diffractometer with $Cu_{K\alpha}$-radiation. The voltage and current applied were 40 kV and 50 mA, respectively. Spectra were collected in the 2θ-range 5-50°. The step time was 4 s and step size was 0.04°. Peak identifications were performed by comparing to standards using the `Diffrac`^{Plus} EVA software from Bruker AXS Inc..

Average size of the silver clusters could have been calculated using the Scherrer equation; however the peaks of the silver at 38.12° (111) overlapped with one of the peaks from the APO_4-5, and made the calculations impossible.

3.3 XAS

X-ray absorption data were collected in the transmission mode at the silver K-edge (25514 eV) at the Swiss Norwegian Beamlines (SNBL, BM01b) using ionization chambers. The ion chambers were filled with the following detector gases: 100% $Ar_{(g)}$ (I_0) and 65% $N_{2\,(g)}$ + 35% $Kr_{(g)}$ (I_t and I_{ref}). ESRF supply electron beam energies of 6 GeV, with a maximum current of 200 mA. The samples were filled in an aluminum sample holder with kapton tape windows yielding a sample thickness of 1-2.5 mm, where the thickness was dependent on the silver content of the samples. The model compounds were mixed with boron nitride, to give a maximal absorber optical thickness of 1.5 absorption lengths. The amount of material used was determined from the silver mass fraction. This was not necessary with the samples, due to their low contents of silver.

Spectra were measured with 5 eV steps below the edge, 0.2 eV steps in the edge region, and steps equivalent to 0.04 $Å^{-1}$ increments above the edge. A number of XAS scans of each sample were recorded and summed. All spectra were energy corrected against a silver-foil calibration (25514 eV).

3.3.1 Testing redox properties

In order to test the samples for their redox properties, the samples were put through an *in-situ* experiment. The samples were placed in an *in-situ* cell, showed in fig. 9.

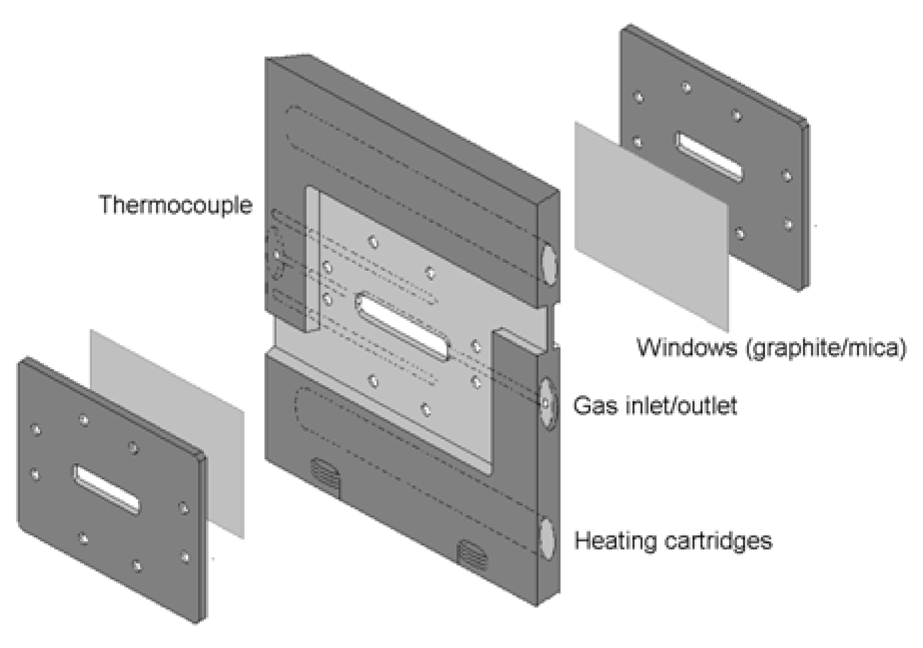

Figure 9: *In-situ-cell for XAS experiments (illustration by Karina Mathisen)*

The sample was loaded into the cell and sealed in place between two graphite and mica windows. The gases could flow directly through the sample, and the heating was acquired by two heating cartridges inserted above and below the sample. The gas flow rate was regulated by flow controllers, and the temperature was measured with a thermocouple inserted into the cell. EXAFS and XANES measurements were recorded during heating and cooling, with different gases flowing through the sample. An *in-situ* experiment usually takes ~12 hours. An outline of the whole setup is shown in fig. 10.

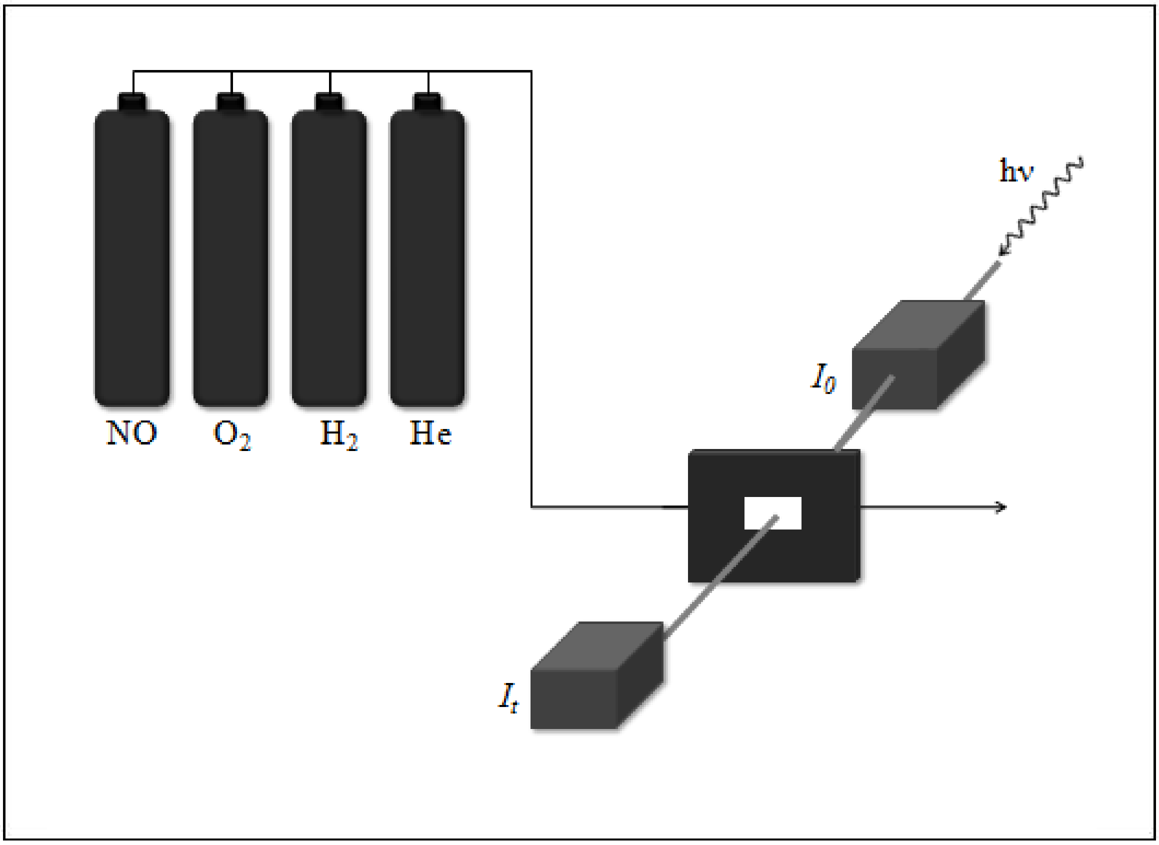

Figure 10: *A sketch of an in-situ setup. The X-ray passes through the first ion chamber to detect the incident intensity (I_0), and then it passes through the sample and finally the second ionic chamber to detect the transmitted intensity (I_t), all while the sample is heated and exposed to different gases.*

Two *in*-situ experiments were preformed; *in-situ* calcination of as-synthesised $AgAPO_4$-5/4 in order to find out when the silver is oxidized during calcination, and a redox *in-situ* of the ion exchanged Ag:SAPO-5 in order to investigate cluster formation.

In the *in-situ* calcination the sample was loaded into the cell to a 3 mm thickness. The sample was heated to 500°C with 5 % O_2 in He (15 mL/min). XANES was recorded continuously during the calcination, while noting the temperature range of each scan.

In the second *in-situ* experiment, Ag:SAPO-5 was loaded into the cell to a 3 mm thickness. The sample was heated in 100 % He (15 mL/min) to 150°C, in order to remove any water present, thus making the pores available for gases passing through. At 150°C, the gas flow was switched to H_2 (15 mL/min), and EXAFS scans were collected at 150°C, 250°C, 350°C and 450°C in H_2. At 450°C, the gas flow was again switched, this time to 50 % O_2 and 50 % NO (15 mL/min), and the sample was cooled to room temperature (RT). XANES were recorded continuously during cooling, and an EXAFS was recorded when at RT. There was no mass spectrometry recording of the exhaust from the *in-situ* experiments due to technical problems.

3.4 ICP-MS

The elemental analysis with ICP-MS was carried out twice, because of the complex composition of the samples. When decomposing the samples with hydrofluoric acid, the aluminium reacted with the fluorine to form a complex, thus the counting of the aluminium content of the samples became far too low. When the samples were decomposed with aqua regia, the silver in the sample precipitated with the chlorine, and the counting of the silver content of the samples became incorrect.

In the first round of analysis, the calcined samples (10-40 mg) were mixed with hydrofluoric acid (0.6 mL, conc., supra pure grade) and nitric acid (1.3 mL, conc., ultra pure grade) in 18 mL vessels of Teflon. The mixture was digested with UltraClave from Milestone with an adjusted time and temperature program (20-250-20°C within 2 hours). The digested samples were diluted with deionised water to 187 mL. The element analysis of the samples was performed using an Element 2 from Thermo Scientific, at medium resolution (R>4000, maximum 5500).

In the second round the same procedure was carried out, only this time the calcined samples were mixed with nitric acid (0.5 mL, conc., supra pure grade) and hydrochloric acid (1.5 mL, conc.), and the digested samples were diluted with deionised water to 220 mL. The rest of the procedure was carried out in the same manner as the first analysis.

The elemental analysis will have more uncertainty due to being performed in two different experiments; however there was no other way to determine the composition of the samples.

3.5 TEM

Transmission electron micrographs were collected with a JEOL 2010F electron microscope, at an acceleration voltage of 200 kV. The samples were suspended in ethanol using an ultrasonic bath, and spread onto a metal grid sample holder coated with a thin layer of carbon. The images were recorded at an acceleration voltage of 200 kV, with magnifications of 60-120 k.

3.6 SEM

The morphology of the products was examined with SEM using a Hitachi S3400N field emission microscope. The samples were dispersed with ethanol on a metal grid sample holder and coated with a thin layer of carbon to make them conductive, to prevent the surface from building up a charge, and thus not come into a sharp image. The images were recorded at an acceleration voltage of 20 kV, with magnifications of 1.9-4.7 k.

3.7 TGA

Thermogravimetric analyses were carried out using a Perkin Elmer Thermogravimetric Analyzer (TGA7). The samples were placed in an Al_2O_3 crucible, and kept under a constant airflow at 80 mL/min. The samples (20-30 mg) were heated to 550°C with temperature rate at 2°C/min. A differential scanning calorimeter (DSC), Jupiter STA 449C, detected endothermic and exothermic reactions, and the connected mass spectrometer, a QMS 403C Aëolos Mass Spectrometer from Netzsch, measured the composition of the outlet gases.

3.8 BET

The samples (0.2-1 g) were carefully weighed in a special designed glass holder, and set to degassing in a VacPrep 061 (Sample Degas System) from Micromeritics for 24 hours at a pressure of 0.1 mbar and temperature of 250°C. Subsequently the dry samples were weighed and the surface area was measured in a Tristar^{TM}3000 from Micromeritics with liquid nitrogen (77 K).

The samples changed colour from white to become beige (Ag:SAPO-5), dark brown (AgAPO$_4$-5/4) and brownish black (Ag:SAPO-11). The AgSAPO-11 was also attempted to be degassed, but it decomposed when heated in vacuum. The powder was “boiling” and was sucked up into the vacuum system. The experiment was not proceeded with this sample in order avoid any equipment being damaged.

Results & Discussion

4.1 General characterization

4.1.1 Structural fingerprint; XRD

The XRD diffractograms of all the as-synthesised and calcined AgAPO$_4$-5’s and AgSAPO-11 are shown in fig. 11 and 12, respectively. They show the fingerprints of the crystal structures of the zeotypes synthesized.

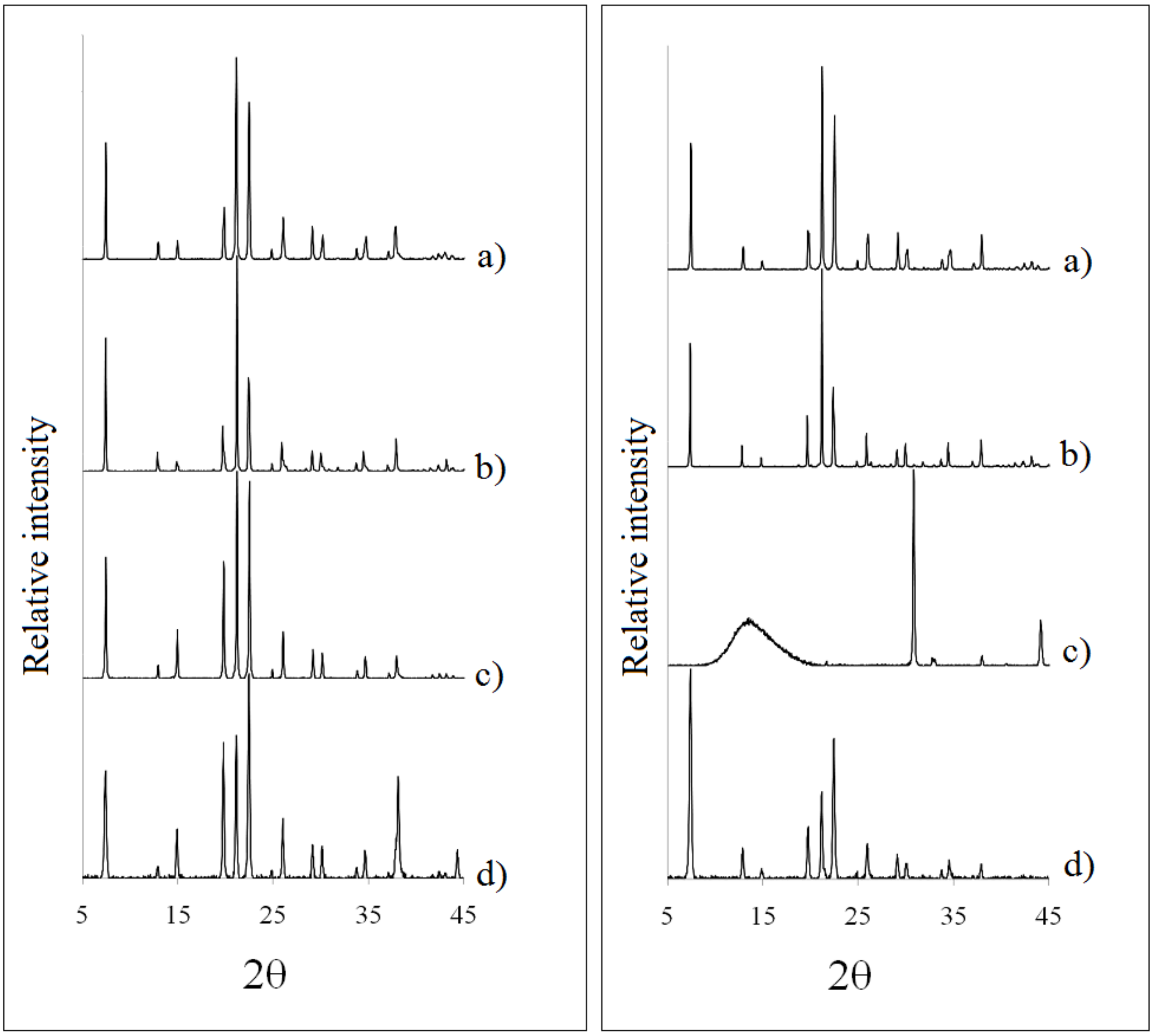

Figure 11: *XRD-diffractograms of the as-synthesised samples (left) and the calcined samples (right): a) AgAPO$_4$-5/1, b) AgAPO$_4$-5/2, c) AgAPO$_4$-5/3 and d) AgAPO$_4$-5/4.*

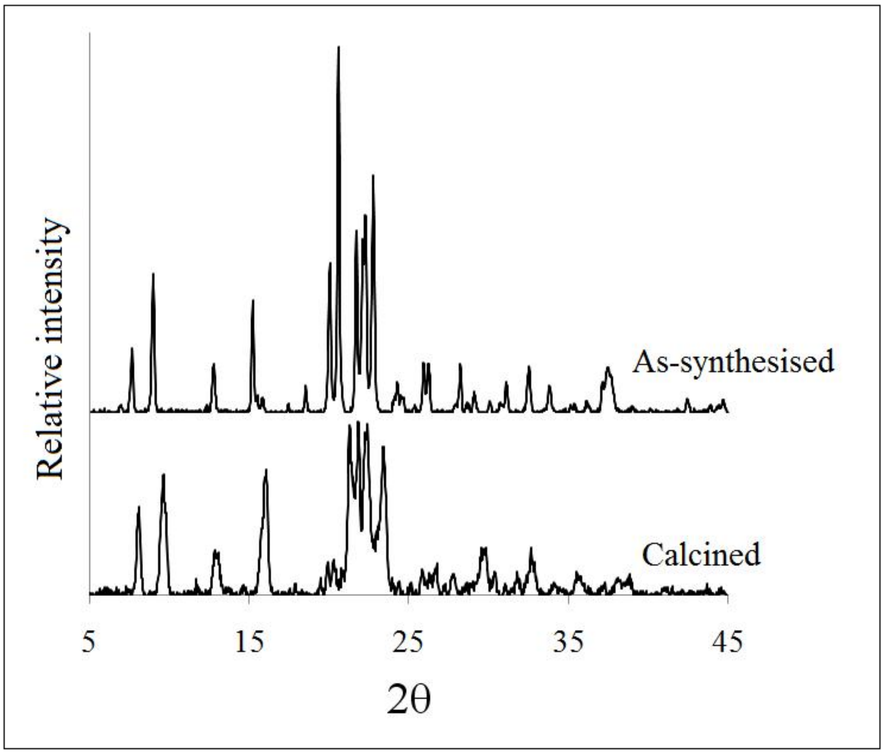

__Figure 12:__ XRD-diffractograms of the as-synthesised and calcined sample of AgSAPO-11.

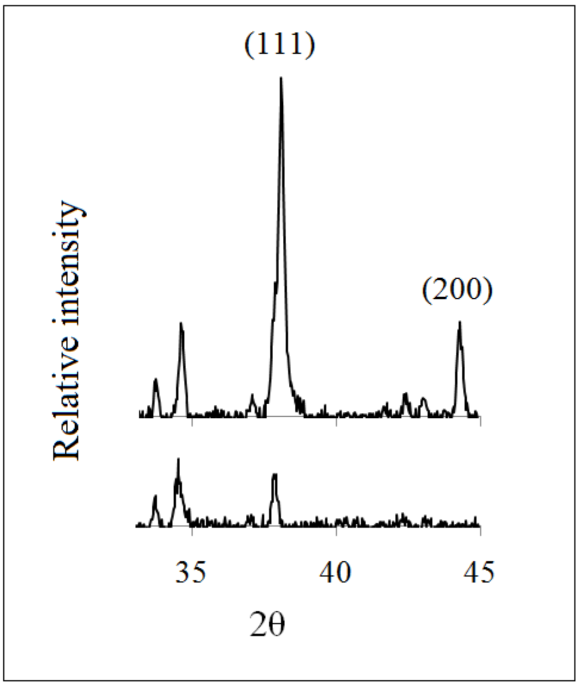

Figure 13: *The silver peaks zoomed in, the upper is as-synthesised AgAPO$_4$-5/4, and the lower is the calcined sample.*

Of all the as-synthesised samples, only $AgAPO_4$-5/4 show the characteristic peaks for silver metal at 38.12° (111) and 44.28° (200), see fig. 13. [32]. These intensities are not apparent in the calcined sample, which suggests the silver being oxidized during calcination. The small peaks at 37.57° in the other samples are due to the (231) diffraction plane in the APO_4-5, and not silver [10]. It can also be seen total collapse of the crystal structure in the calcined sample of $AgAPO_4$-5/3, and a partial collapse of the calcined AgSAPO-11. The fact that silver is in the metallic state in the as-synthesised $AgAPO_4$-5/4, tells us that it is not incorporated into the framework of the microporous zeotypes. It is reasonable to believe that the silver is metallic in the other samples too, due to the brown colour of the products, even though the silver is not shown in the diffractograms.

With the attempt to synthesize several samples at a lower crystallization temperature, all the samples came out amorphous in the XRD fingerprint. The temperature of 100°C was probably not high enough for the crystallization to occur, or 24 h was not enough time for the crystallization to take place at this temperature.

In the experiment where the samples were taken out after 1, 2, 3 and 4 hours, they all turned out to be amorphous in the diffractograms and the dark colour indicates metallic silver. This tells us that silver is autoreduced before the crystallization of the framework, thus silver cannot incorporate into the framework. Michalik et al. (1995) claim to have incorporated silver into a SAPO-11 framework in a hydrothermal synthesis, giving a yellow-green product [9]. The recipe used in the synthesis of the AgSAPO-11 in this thesis is the same one they used, however the product in this synthesis became brown, thus probably containing metallic silver.

4.1.2 Composition; ICP-MS

The results from ICP-MS measurements of all the samples are shown in table 2. The silver contents of the samples range from 0.006 wt% to 4.9 wt %, which gives a perspective of how much silver is attached to the microporous carrier. In the first three $AgAPO_4$-5 samples, the silver content is quite low, compared to the Ag:Al ratio from the syntheses (table 1, chap. 3.1). This is probably an explanation of why the silver metal was not apparent in the diffractograms of these samples. The amine groups in the template can act as a complexing agent with silver [33], thus the template which is added to obtain the unique crystal structure is preventing the silver from being incorporated into the framework. In addition there is the fact that silver is autoreduced before the crystallization of the framework.

Table 2: *Summary of the results from ICP-MS measurements, including the calculated molar ratio of Ag:Al, and molar composition of the samples.*

Sample	**Al wt%**	**Si wt%**	**P wt%**	**Ag wt%**	**Ag:Al (mole)**	**Molar composition**
AgAPO$_4$-5/1	21.5	-	23.2	0.00670	$7.79*10^{-5}$	$Ag_{0.0000078}AlP_{0.94}O_4$
AgAPO$_4$-5/2	25.3	-	28.6	0.0138	0.000136	$Ag_{0.00014}AlP_{0.99}O_4$
AgAPO$_4$-5/3	24.0	-	23.1	0.0118	0.000123	$Ag_{0.00012}AlP_{0.84}O_4$
AgAPO$_4$-5/4	27.7	-	16.2	4.89	0.0441	$Ag_{0.044}AlP_{0.51}O_4$
AgSAPO-11	19.9	0.911	23.3	2.89	0.0371	$Ag_{0.037}Si_{0.045}AlP_{1.04}O_4$
Ag:SAPO-5	18.1	0.559	18.2	4.15	0.0573	$Ag_{0.057}Si_{0.030}AlP_{0.87}O_4$
Ag:SAPO-11	22.7	1.00	21.5	2.77	0.0306	$Ag_{0.030}Si_{0.042}AlP_{0.82}O_4$

Whether the template has anything to do with the reduction of silver is not clear. However, You et al. (2009) synthesised silver nanowires with dodecylamine, and they claim that the complexing of the nitrogen lone pairs with silver(I) will reduce the silver upon heating (100°C) [33]. If this is the case with the templates used in the syntheses in this thesis (they are all amines), then it might be the template causing the reduction of the silver, and not only the high temperature and pressure in the autoclave. Even though Pauley et al. (1966) report that silver-amine complexes of tertiary amines are much less stable than primary and secondary amines [13], it seem the complexing is still happening with TEA (tertiary amine), resulting in the low silver content of the samples made with TEA. The silver-amine complexes are probably washed out of the sample after crystallization when the sample is washed with deionised water.

In AgAPO$_4$-5/4, the silver content of the sample is close to that of the synthesis, which indicates the silver being attached to the APO$_4$-5 framework in some way. It seems that the combination of silver(I) sulphate and MDCHA makes the silver attach to the APO$_4$-5 and not complex with the template in the same degree at the first three samples. However, the reason for the higher silver content in this sample might also be a result of a miscalculation of the recipe, thus adding far too little orthophosphoric acid (P:Al ratio 0.51). Strangely, the X-ray diffractograms of this sample show the exact same APO$_4$-5 crystal structure as the other samples, even though there is almost half the amount phosphorous as it should have been. This miscalculation is most likely the reason for the larger silver content, rather than the combination of the template and silver source. To be able to verify this, one could have made the $AgAPO_4$-5/4 one more time with the right amount of orthophosphoric acid, and perform an elemental analysis of this sample.

4.1.3 Surface area; BET

The results from the BET surface area measurements are presented in table 3. The observation of the white powders becoming brown suggests that the silver was reduced upon heating in vacuum. Why this happened is not clear, but it may be suggested that when the oxidising atmosphere of air was removed, the silver reacted due to the heating, and became reduced.

The surface area of $AgAPO_4$-5/4 is close to that of APO_4-5 which is 254 m^2/g [34]. The surface area of Ag:SAPO-5 is significantly smaller than reported for SAPO-5 in literature, which is 249 m^2/g [35]. The Ag:SAPO-11 on the other hand, is close to that of pure SAPO-11, which is reported to be 185 m^2/g [36].

Table 3: *Results from the surface area measurements with BET.*

Sample	**Surface area, m^2/g**
$AgAPO_4$-5/4	216 (3)
Ag:SAPO-5	141 (3)
Ag:SAPO-11	169 (3)

The reason for the lower surface area in the samples compared to the pure APO-5 and SAPO's, might be explained by the possibly reduced silver. The silver clusters formed may be clogging the pores of the microporous structure, thus the adsorbing gas was hindered to flow into the structure and adsorb on the surface. However, the use of BET to measure the inner surface area of zeolites and zeotypes may involve large uncertainties, due to the fact that the method originally is applicable for materials with pores larger than 4 nm [28].

4.1.4 Morphology and cluster size; SEM and TEM

The SEM images of $AgAPO_4$-5/4 shown in fig. 14, and images of AgSAPO-11 are shown in fig. 15.

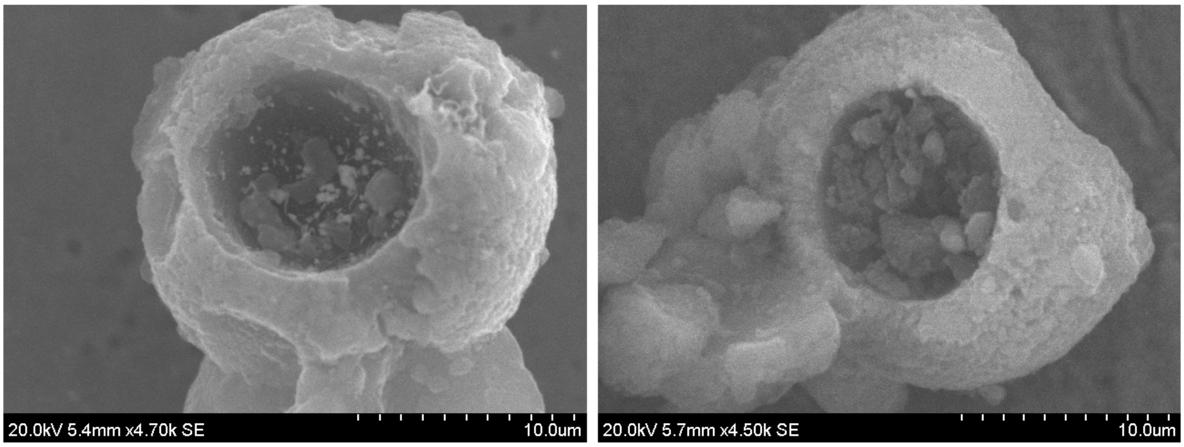

Figure 14: *Scanning electron micrographs of AgAPO$_4$-5/4, as-synthesised (left) and calcined (right).*

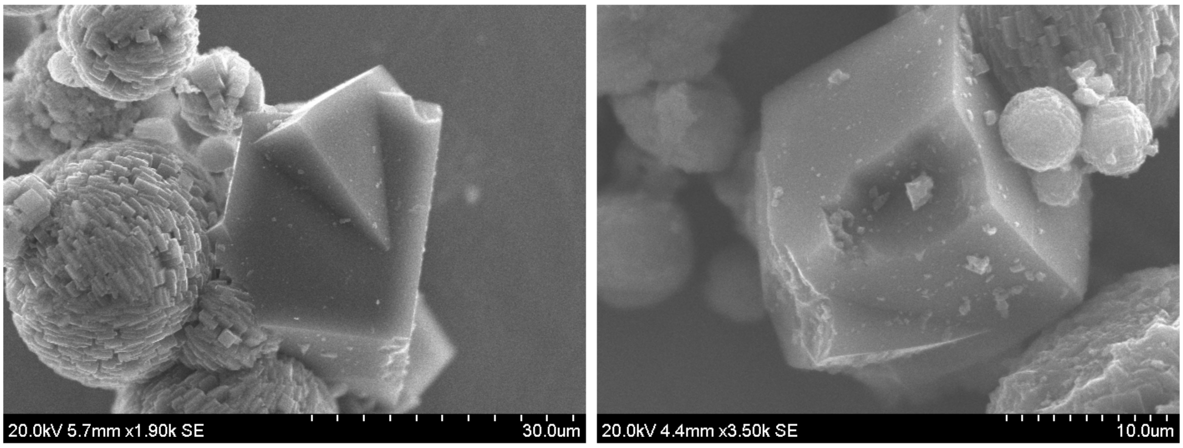

Figure 15: *Scanning electron micrographs of AgSAPO-11, as-synthesised (left) and calcined (right).*

The SEM of AgSAPO-11 show large cubic single crystals, and large aggregates of cubic crystallites. The crystal in the image of the as-synthesised sample is ca 23 µm wide (horizontal). Even though the XRD show a partial breakdown of the framework in AgSAPO-11, the SEM show that the cubic crystals are still there. The cubic crystals are consistent with the findings of Shengzhen et al. (2007), who report that SAPO-11 mostly consist of pseudo-spherical aggregates ranging from 3 to 10 µm in size, and that is has cubic crystals and crystallites [37]. The AgAPO$_4$-5/4 did not show any sign of single crystals, only large aggregates (3 to 15 µm in size) of crystallites.

The TEM images of AgAPO$_4$-5/2a and AgAPO$_4$-5/3a are shown in fig. 16 and 17 respectively. It can clearly be seen that the particles of the AgAPO$_4$-5/2a have a hexagonal shape in fig. 16, and that there are various phases in the sample, both crystals and aggregates. The particle in image d in fig. 16 is 3.6 µm from face to face across the crystal, 4 µm from corner to corner and the sides are ca 2 µm.

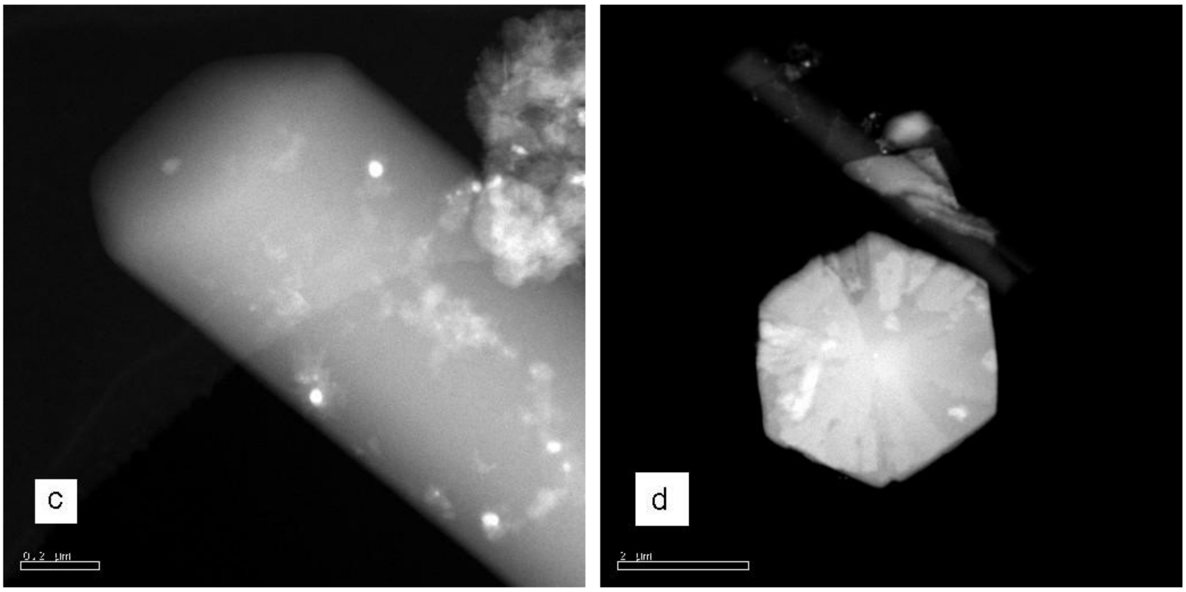

Figure 16: *Transmission electron micrographs of AgAPO$_4$-5/2a.*

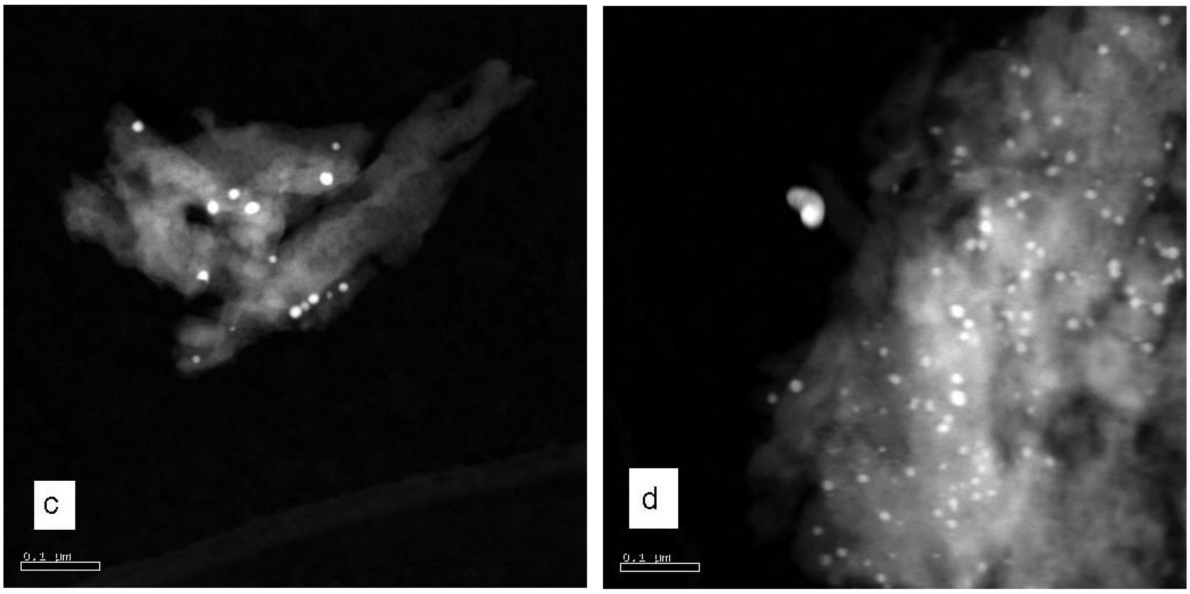

Figure 17: *Transmission electron micrographs of AgAPO$_4$-5/3a.*

The images of AgAPO$_4$-5/3a in fig. 17 gave an opportunity to measure the sizes of the silver clusters in this sample, and a summary of the statistics is given in fig. 18. The clusters range from 6 nm to 29 nm in size, but the main distribution is 12-18 nm. The mean cluster size is 12.8 nm. These are quite small nano clusters, but they are too big to fit into the pores of the microporous APO$_4$-5, thus the silver has to be on the outside surface of the crystallites. The AgAPO$_4$-5/3a does not show the same type of hexagonal crystal like AgAPO$_4$-5/2a does, but is probably in the form of aggregated crystallites, similar to the aggregates seen in fig. 14.

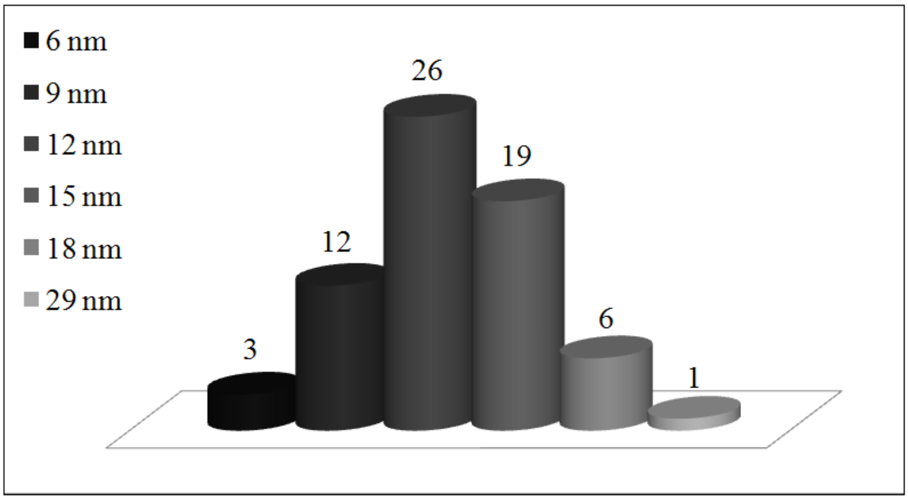

Figure 18: *Histogram of the size of the clusters in AgAPO$_4$-5/3a.*

4.1.5 Thermal analysis; TGA

The TGA results for AgAPO$_4$-5/4 and AgSAPO-11 are shown in fig. 19 and 20, respectively. The results give information about how the samples lose weight as they are heated during calcination. The mass spectrometry results are displayed in Appendix A, and the molar masses detected in the outlet of both samples were 2, 12, 16, 18, 28, 40, 44, 46 and 64 amu.

In the AgAPO$_4$-5/4, there is a small endothermic reaction and weight loss at 25-70°C due to water removal, giving a mass loss of 1.4 %. The exothermic reaction at 170-340°C is probably due to decomposition or burn off of the template, with a mass loss of 7.8 %. This is consistent with the findings of Roldán et al. (2007), who performed TGA on a sample made with the same template (MDCHA) [38]. The mass spectrographs show an increase in the molar masses of 12, 18, 28, 32, 40, 44, 46 amu in this temperature range. The most probable identities of these masses are carbon (12 amu), water (18 amu), CO/N_2 (28 amu), oxygen (32 amu), argon (40 amu), CO_2/N_2O (44 amu), and NO_2 (46 amu). The last exothermic reaction at 380-440°C is probably due to more burn off of the remnants of the template, however the mass spectrograms do not show any clear signs of what this might be. There is a slight increase in carbon (12 amu), water (18 amu), CO_2/N_2O (44 amu), and NO_2 (46 amu). The mass loss in this temperature range is 8.0 %, and the total mass loss is 23%.

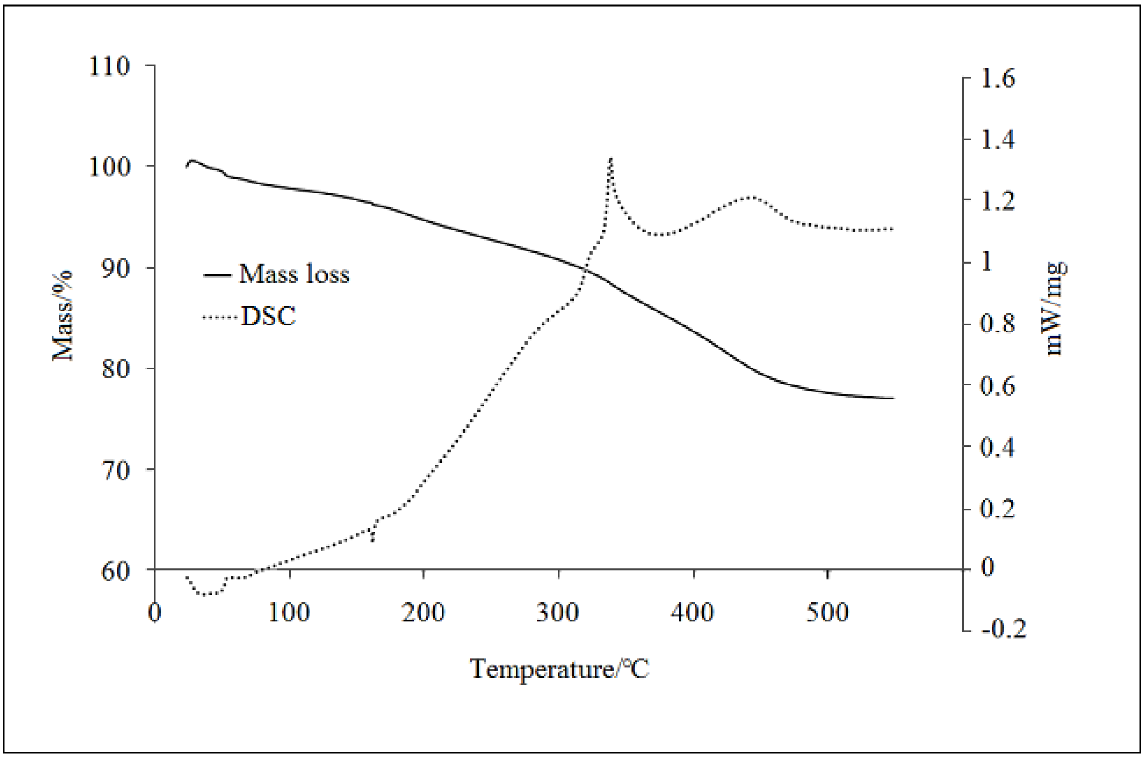

Figure 19: *TGA and DSC of AgAPO$_4$-5/4.*

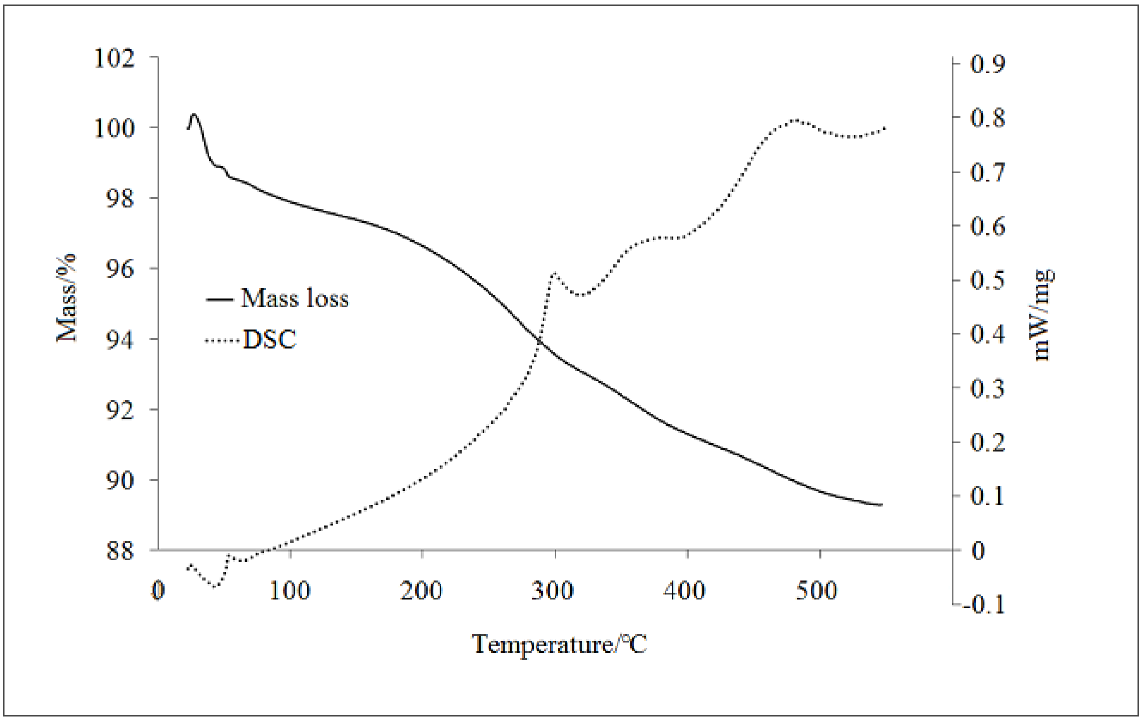

Figure 20: *TGA and DSC of AgSAPO-11.*

In AgSAPO-11 it also looks like some water goes off in the beginning as an endothermic reaction, however the mass spectrometers do not show any signs of this. The mass loss in the first temperature range (25-170°C) is 2.9 %. The template seems to burn off at 170-280°C, which is consistent with the findings of Gao et al. (1996) who performed TGA on a sample made with the same template (i-Pr_2NH) [39]. The mass spectrograms show an increase in the molar masses of 2, 12, 16, 18, 28, 32, 40 and 44 amu. The identities of the molar masses 12, 18, 28, 32, 40 and 44 amu are probably the same as in $AgAPO_4$-5/4, and the identity of 2 and 16 are probably hydrogen and ammonia or methane, respectively. The mass loss in this temperature range is 2.9 %. In the last temperature range of the graph, 280-550°C, there is a mass loss of 4.9 %, giving a total mass loss of 10.7 %. The last mass loss is probably due to additional decomposition of the template. Some of the template may be fixed at the cation sites in the SAPO-11 framework, thus making it harder to remove. The mass spectrographs show a small increase in carbon (12 amu) and CO_2/N_2O (44 amu) in this last temperature range. There may however be another explanation for this exothermic reaction; decomposition of the SAPO-11 framework. The X-ray diffractograms of the AgSAPO-11 indicated a partial breakdown of the SAPO-11 framework, and this would be an exothermic reaction. It would have been interesting to collect a XRD of the AgSAPO-11 after the TGA, to find out if it was decomposed from the treatment. If this was the case, it would indicate that the template decomposed at a far lower temperature than 550°C, and the calcining of the sample could be performed at a lower temperature to prevent the lattice from breaking down.

4.2 Structural characterization; XAS

4.2.1 Models

It has been common to use silver(I) oxide as a model for samples containing ionic silver(I). In EXAFS analysis this is reasonable, because the model only need to be in the same oxidation state for the AFAC to be transferable. However, in XANES analysis, one usually compares the shape of the spectrum to suggest conclusions about the oxidation states and the local environment surrounding the absorbing atom in the samples. When the XANES of silver(I) oxide does not look like the calcined samples (which are assumed to contain mostly silver(I) species), one has to look elsewhere for a suitable model. Thus, XANES of several silver(I) salts and solutions were recorded. The result showed silver (I) sulphate to be the best model to compare the calcined samples with. This result is visualized in fig. 21, where both silver(I) oxide and silver(I) sulphate are compared to the calcined sample, in addition to a comparison of as-synthesised sample and the foil. The structural values obtained from EXAFS analysis of the models are displayed in table 4.

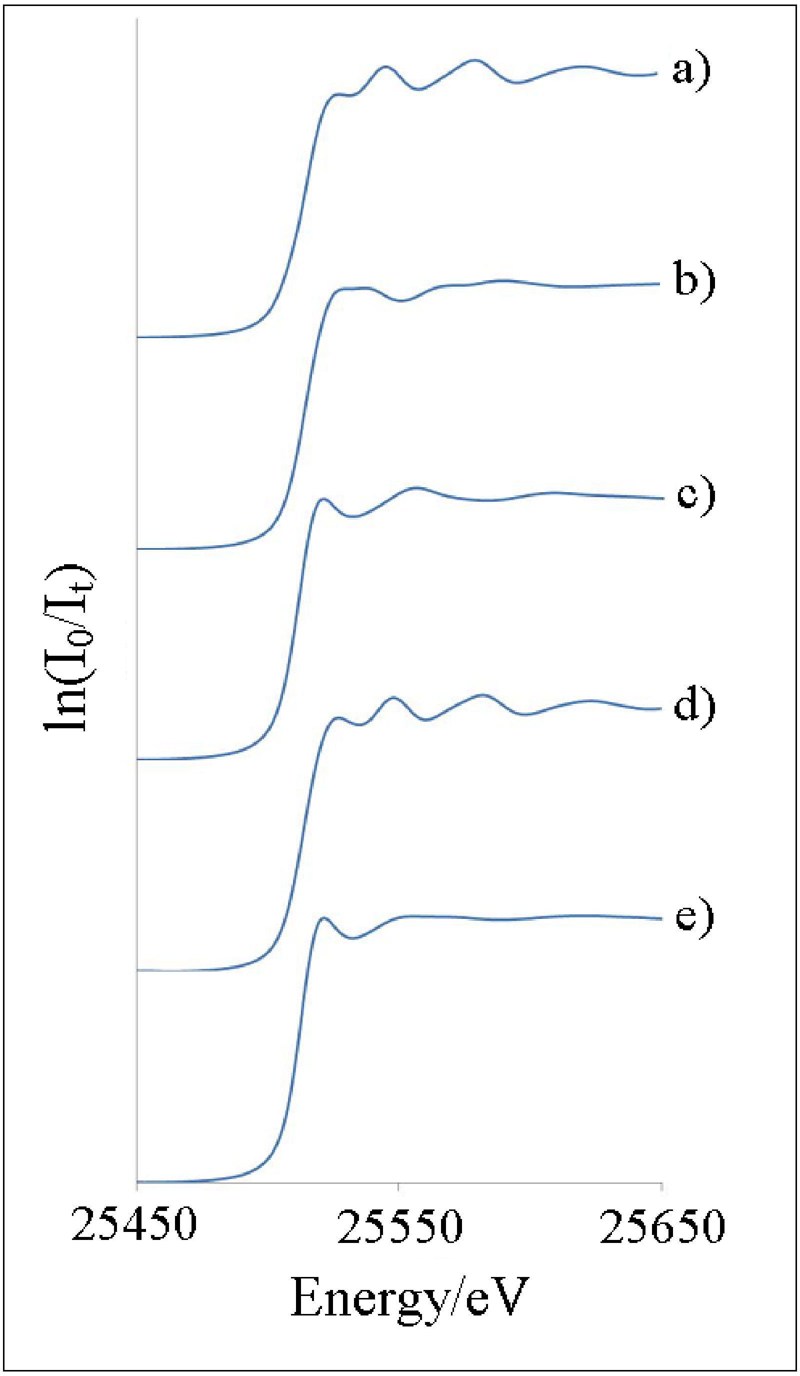

Figure 21: *Normalized XANES of a) silver (0) foil, b) silver(I) oxide, c) silver(I) sulphate, d) as-synthesised sample of AgAPO*$_4$*-5/4 and e) calcined sample of AgAPO*$_4$*-5/4.*

***Table 4: Models** Parameters from the least square EXAFS analysis for Ag^0-foil, Ag_2O and Ag_2SO_4, used as model compounds for analysis of the Ag K-edge data for the samples.*

Sample	**Shell**	**N**	**r/(Å)**	**r, XRD (Å)**	**$2\sigma^2/(Å^2)$**	**R/(%)**	**Ef**	**AFAC**
Ag^0-foil	Ag-Ag	12^1	2.876 (4)	2.889^1	0.0176 (8)	26.21	-3.8 (5)	0.65 (2)
Ag_2O	Ag-O	2.0^2	2.080 (5)	2.043^1	0.010 (1)	23.62	-6.2 (6)	0.6863
	Ag···Ag	12.0^1	3.31 (3)	3.336^1	0.076 (9)			
	Ag···O	6.0^2	3.56 (5)	3.90^2	0.05 (2)			
Ag_2SO_4	Ag-O	1.62 (7)	2.315 (8)		0.003 (2)	24.19	-3.0 (5)	0.6863
	Ag-O, 2nd	2.4 (1)	2.48 (1)		0.011 (3)			
	Ag···Ag	2.5 (7)	4.34 (3)		0.026 (9)			
	Ag···S	2.4 (7)	4.53 (3)		0.02 (1)			

[1] known from Bailar et al. [12]
[2] known from Houde-Walter [40]
N – multiplicity
r – binding distance
$2\sigma^2$ – Debye-Waller factor
R – fit factor
Ef – refined correction of Fermi energy

The two different oxygen shells in the sulphate is consistent with the findings of Levy et al. (1978) and Shimizu et al. (2001), who report that the silver(I) ion in silver(I) sulphate is surrounded by six oxygen atoms at 2.4-2.6 Å distance [16; 41]. The oxygen multiplicities of the sulphate from this refinement are however too low (~4) to be six oxygen atoms. Several attempts to fit different coordinations, both in number and type were carried out; however, the presented result gave the best fit with relatively low standard deviations and reasonable Debye-Waller factors. There seem to be some confusion about the structure of silver(I) sulphate in the literature, because Robbins et al. (1977) report that silver is five coordinated by oxygen atoms in silver(I) sulphate, along with a zig-zag structure of the silver ions giving a Ag···Ag distance of 3.3 Å [42]. This is not consistent with the findings of Levy et al. (1978) and Shimizu et al. (2001), or the Ag···Ag of r = 4.34 Å from this refinement. As it has not been discovered any literature where EXAFS of silver(I) sulphate has been collected [5], and as the literature is contradictory about the structure, a proposal of the structure have been made, presented in fig. 22.

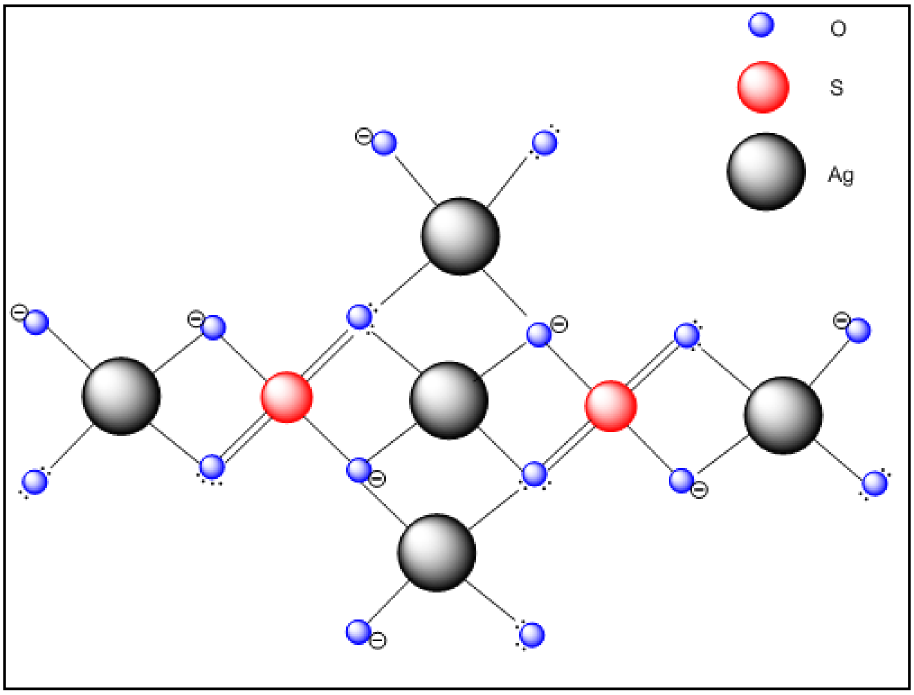

Figure 22: *A sketch of the proposed structure of silver(I) sulphate.*

It must be emphasized that the proposed structure is merely based on the EXAFS results and the following reasoning about the bonding in the structure:

- ✓ The relative angles, distances and number of atoms of each type in the sketch are not supposed to be structurally truthful.
- ✓ The proposed structure shows that there are two different oxygen shells, with in all four oxygen atoms, and that there are two silver atoms and two sulphur atoms within similar distance (4.34 Å and 4.53 Å respectively).
- ✓ It is suggested that the two independent shells of oxygen are due to two different kinds of oxygen atoms bound to the silver atom:
    - The sulphate has two oxygen atoms bound with a single bond. These negatively charged oxygen atoms are suggested to be in a resonance structure where they share their one electron between two silver atoms, and that each silver atom is bound to two of these "bridging" oxygen atoms. This type of binding geometry is well known from the diborane

---

[5] Shibata et al. (2004) and Shimizu et al. (2001; 2007a; 2007b) have used XANES of silver(I) sulphate as a model for ionic silver(I) [17; 16; 3; 44], but they do not report any EXAFS results for the compound.

molecule, and is sometimes referred to as “banana bonding” [43]. These oxygen atoms are believed to be in the first shell of oxygen atoms (2.315 Å) in the silver(I) sulphate.

- The sulphate has two oxygen atoms bound with double bonds. These oxygen atoms have no charge; they do however have two lone pairs. One of these lone pairs can be donated to the silver atom. It is suggested that the silver is “bound” to two of these oxygen atoms, which constitute the second shell of oxygen atoms (2.48 Å) in the silver(I) sulphate.

4.2.2 Samples

Normalized XANES of all the as-synthesised samples are shown in fig. 23 where they are compared to the silver(0) foil, and all the calcined samples are in fig. 24, compared to silver(I) sulphate. The environment surrounding the silver ions in silver(I) sulphate seem to resemble the environment in the calcined samples, thus the sulphate has been used as a XANES model for the calcined samples.

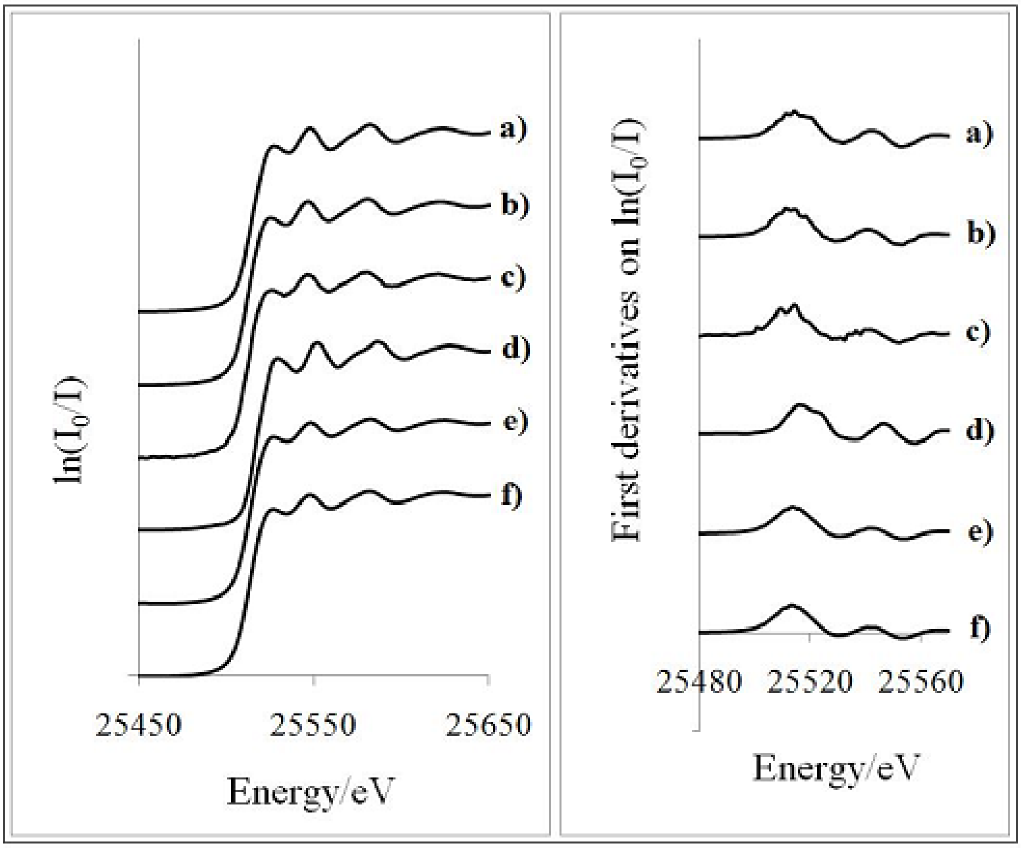

Figure 23 *Left: Normalized XANES of a) silver(0) foil, b) AgAPO$_4$-5/1, c) AgAPO$_4$-5/2, d) AgAPO$_4$-5/3, e) AgAPO$_4$-5/4 and f) AgSAPO-11, all as-synthesised. Right: the first derivatives of μ(E).*

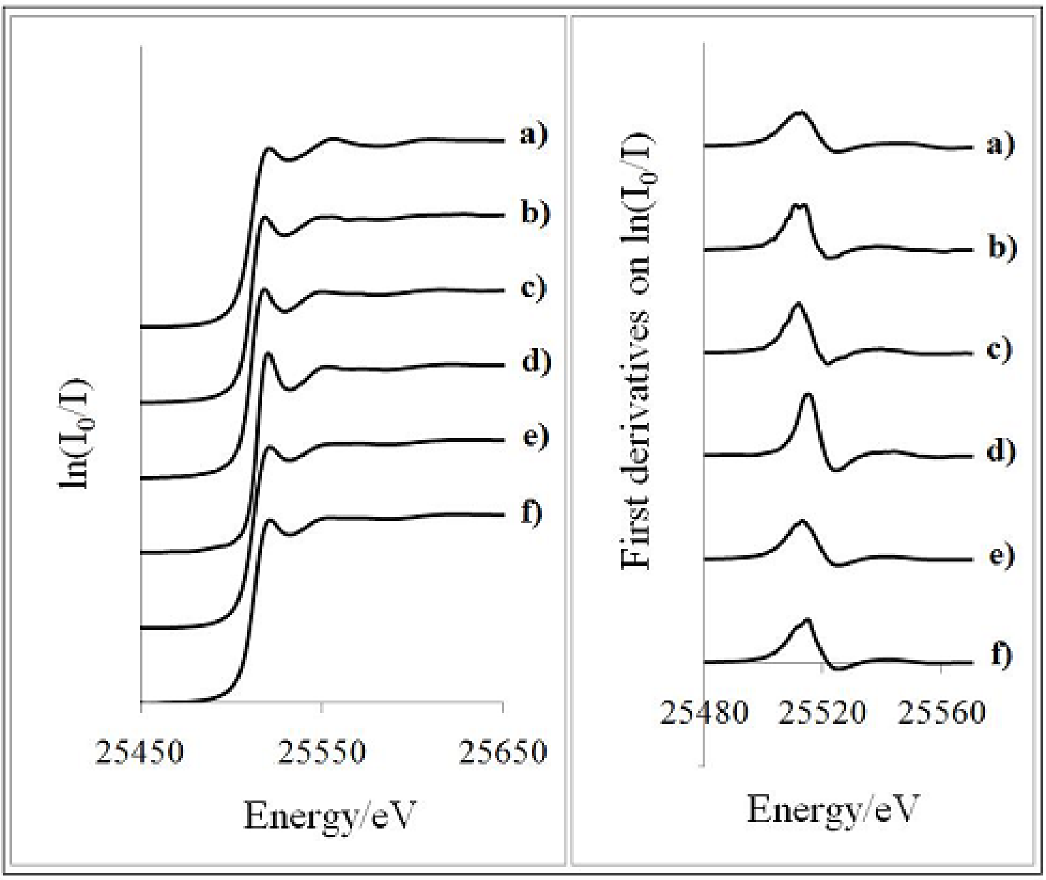

Figure 24 *Left: Normalized XANES of a) silver(0) foil, b) AgAPO*$_4$*-5/1, c) AgAPO*$_4$*-5/2, d) AgAPO*$_4$*-5/3, e) AgAPO*$_4$*-5/4 and f) AgSAPO-11, all as-synthesised. Right: the first derivatives of μ(E).*

The XANES models, silver(0) foil and silver(I) sulphate, were used in the linear combination fit to investigate the distribution of the silver species in all the samples. The results are shown in fig. 25. It can clearly be seen that metallic silver(0) is most abundant in the as-synthesised samples, and that the silver in the calcined samples is fully oxidized. These results are consistent with the results from XRD and XANES. The numerical values from the linear combination can be found in Appendix B.

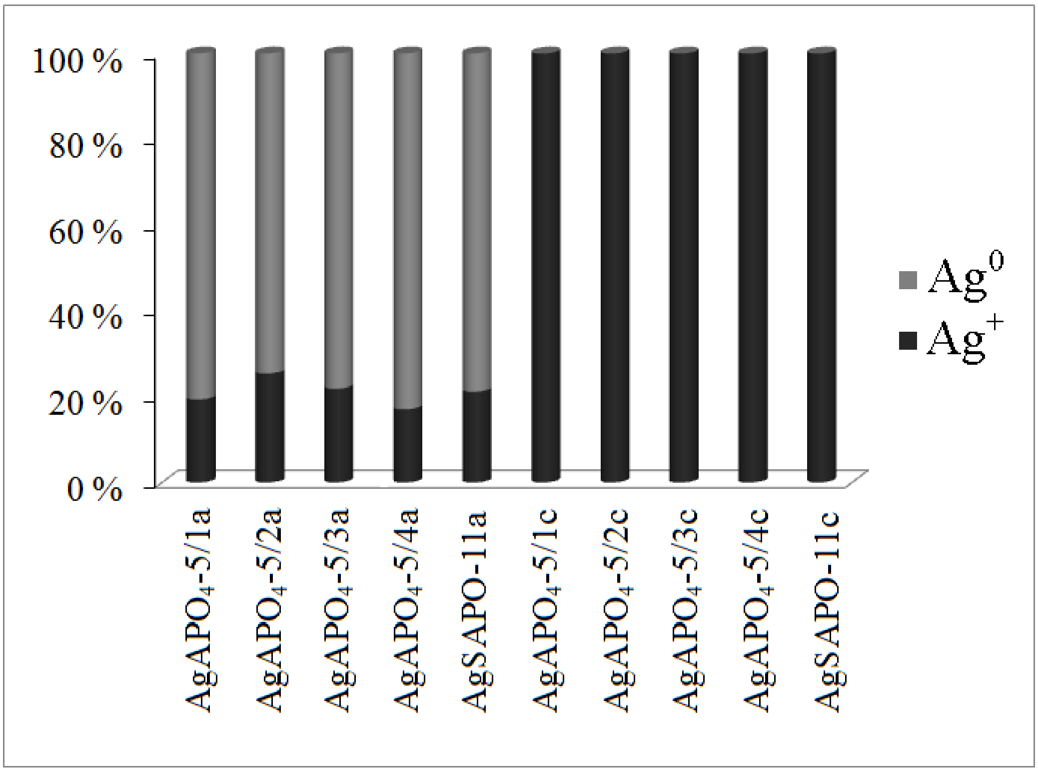

Figure 25: *Percentage of ionic Ag(I) and metallic Ag(0) species in the samples. The letter "a" indicates as-synthesised, and the letter "c" indicates calcined.*

The graphical results from EXAFS analysis of the as-synthesised and the calcined samples are displayed in fig. 26 and 27, respectively, and the structural parameters from the refinements are presented in table 5. The EXAFS of the as-synthesised samples are similar in shape and all looks like the EXAFS of the foil. The FTs show that the binding distances are the same. However, the refined parameters in table 5 show that the binding distances in the samples are somewhat smaller than that of the foil. This suggests that the lattice has shrunk due to the clusters being small. The multiplicities are relatively high (close to 12), which indicates that the bulk lattice structure is maintained. This is consistent with the findings of George et al. (1992) who, as previously mentioned, found that shrinkage of the lattice constant (and thus the binding distances) in small clusters did not change the fcc-lattice of the silver [14]. The clusters may however have different properties from the silver bulk, due to the small size, indicated by the shorter binding distance. The size of the clusters will be discussed more thorough in a later section.

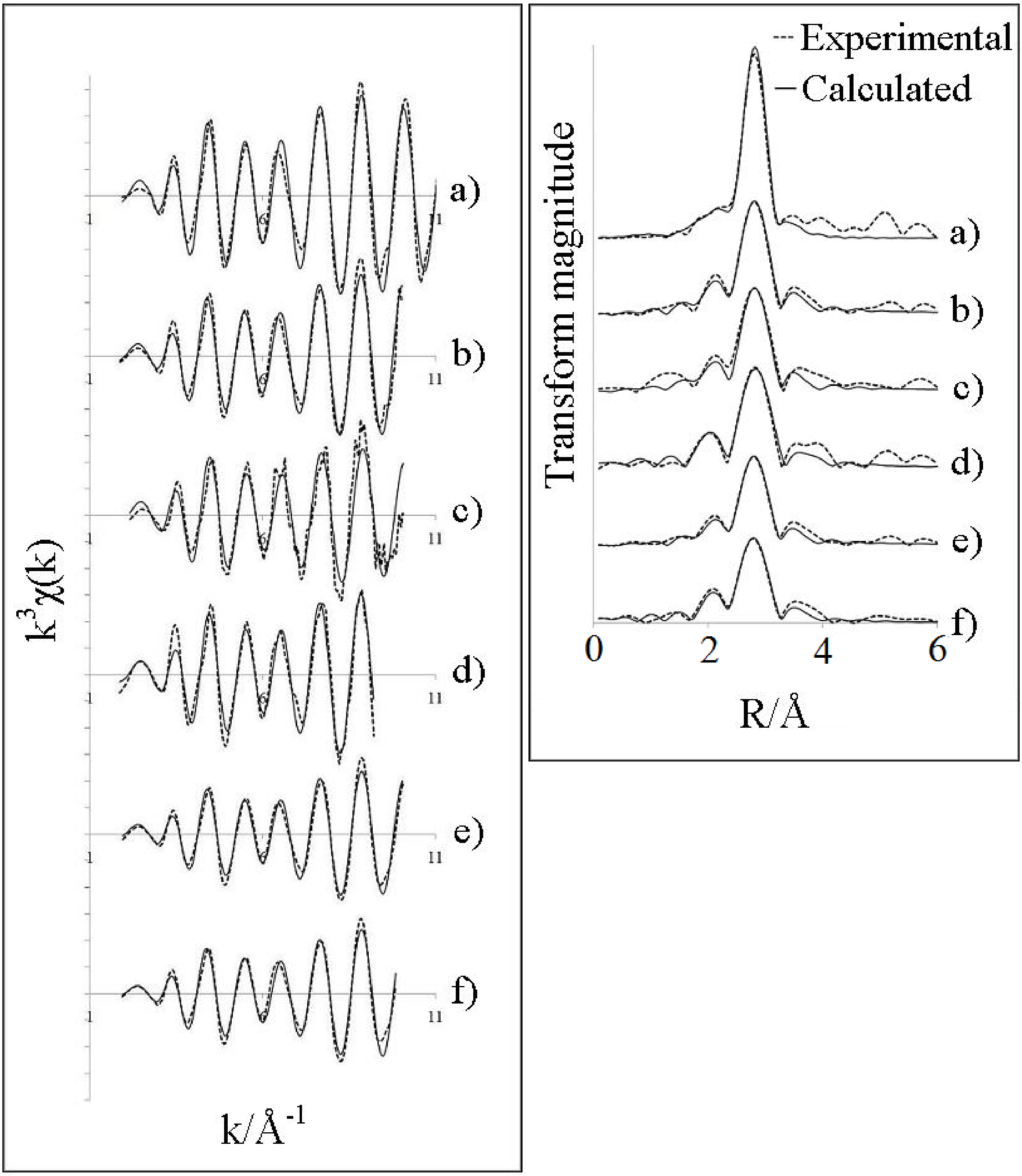

Figure 26 *Left: k^3-weighted EXAFS for a) silver(0) foil, b) $AgAPO_4$-5/1, c) $AgAPO_4$-5/2, d) $AgAPO_4$-5/3, e) $AgAPO_4$-5/4 and f) AgSAPO-11, all as-synthesised. Right: Experimental and calculated Fourier Transforms of the same samples.*

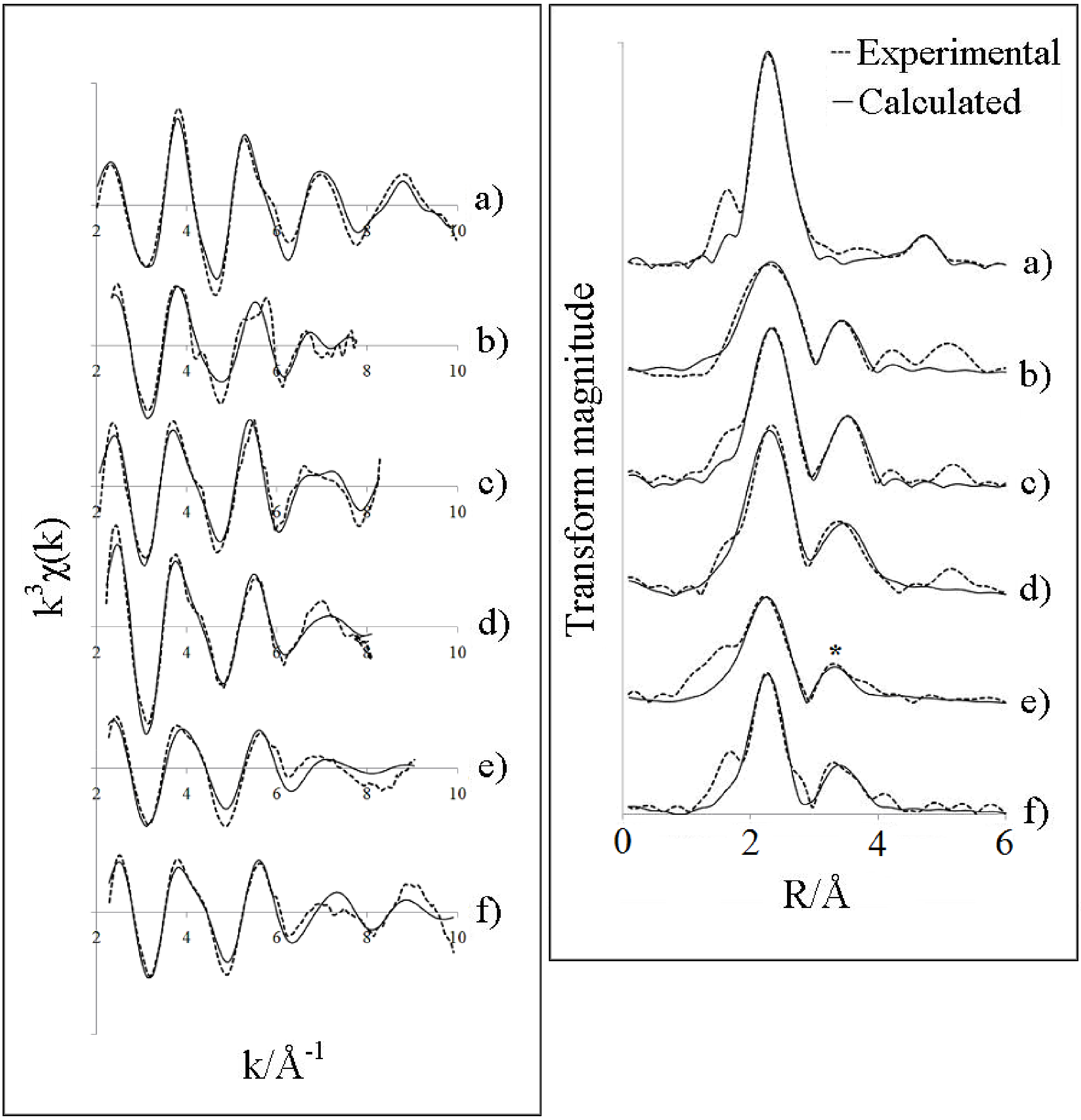

Figure 27 *Left:* k^3*-weighted EXAFS for a) silver(I) sulphate, b)* $AgAPO_4$*-5/1, c)* $AgAPO_4$*-5/2, d)* $AgAPO_4$*-5/3, e)* $AgAPO_4$*-5/4 and f) AgSAPO-11, all calcined. Right: Experimental and calculated Fourier Transforms of the same samples.*

***Table 5: Samples** Parameters from the least squares EXAFS analysis of the $AgAPO_4$-5 samples and the AgSAPO-11.*

Sample	**Shell**	**N**	**r/(Å)**	**$2\sigma^2/(Å^2)$**	**R/(%)**	**Ef**	**AFAC**	**Δk**
$AgAPO_4$-5/1a	Ag-Ag	10.7 (9)	2.868 (4)	0.020 (1)	22.46	-3.5 (5)	0.8165	2 – 10
$AgAPO_4$-5/2a	Ag-Ag	10.3 (7)	2.856 (5)	0.022 (1)	39.64	-1.9 (6)	0.8165	1 – 15
$AgAPO_4$-5/3a	Ag-Ag	11.7 (6)	2.882 (3)	0.0206 (9)	27.09	-8.6 (4)	0.8096	2 – 9.5
$AgAPO_4$-5/4a	Ag-Ag	10.5 (8)	2.859 (3)	0.020 (1)	20.60	-4.9 (5)	0.65	2 – 10
AgSAPO-11a	Ag-Ag	9.5 (8)	2.854 (4)	0.018 (1)	20.57	-5.6 (5)	0.65	2 – 10
$AgAPO_4$-5/1c	Ag-O	3.8 (6)	2.39 (1)	0.055 (8)	29.88	0.2 (7)	0.903	2 – 9
	Ag···O	1.8 (8)	3.46 (2)	0.02 (1)				
$AgAPO_4$-5/2c	Ag-O	2.9 (3)	2.408 (9)	0.032 (4)	26.37	-1.2 (5)	0.903	2 – 10
	Ag···O	4 (1)	3.55 (2)	0.030 (10)				
$AgAPO_4$-5/3c	Ag-O	4.7 (4)	2.378 (10)	0.051 (5)	19.15	-0.8 (4)	0.8377	1.7 – 8
	Ag···O	11 (3)	3.52 (2)	0.07 (2)				
$AgAPO_4$-5/4c	Ag-O	3.9 (2)	2.345 (8)	0.048 (3)	36.36	-2.2 (4)	0.6863	2.2 – 9
	Ag···Al	4.5 (9)	3.26 (3)	0.07 (1)				
AgSAPO-11c	Ag-O	2.7 (3)	2.324 (9)	0.027 (4)	28.68	-0.0 (5)	0.6863	2 – 10
	Ag···O	7 (2)	3.46 (3)	0.06 (2)				

The EXAFS of the calcined samples look similar to that of silver(I) sulphate, but the FTs are somewhat different from the sulphate, as the second shell of oxygen atoms are at a longer distance from the silver in the samples. However, as the XANES are similar to that of the sulphate, and the fact that there are oxygen, not silver in the second shell, we believe that the environment around the silver(I) in the calcined samples are similar to that of the silver(I) in the sulphate. The N- and r-values of the first shells of oxygen varies to some extent, but they are consistent with the findings of Shimizu et al. (2007a), who found 1.6-5.3 oxygen atoms at a distance 2.48-2.52 Å (in a Ag/Al_2O_3 catalyst under varying atmosphere) [3]. However in their results the second shell contained silver and not oxygen, and as the sample is not of the same nature as the ones in this thesis, the results are not directly comparable.

The FTs of the calcined samples are similar to each other, and they all have two separate shells of oxygen, except $AgAPO_4$-5/4. This sample seems to have aluminium in the second shell. The spectrum was difficult to fit, and in order to investigate the identity of the elements in the second shell, the second to in the FT was Fourier Filtered (FF), see fig. 28. All the other samples were also Fourier Filtered, and their FF-graphs are found in Appendix C.

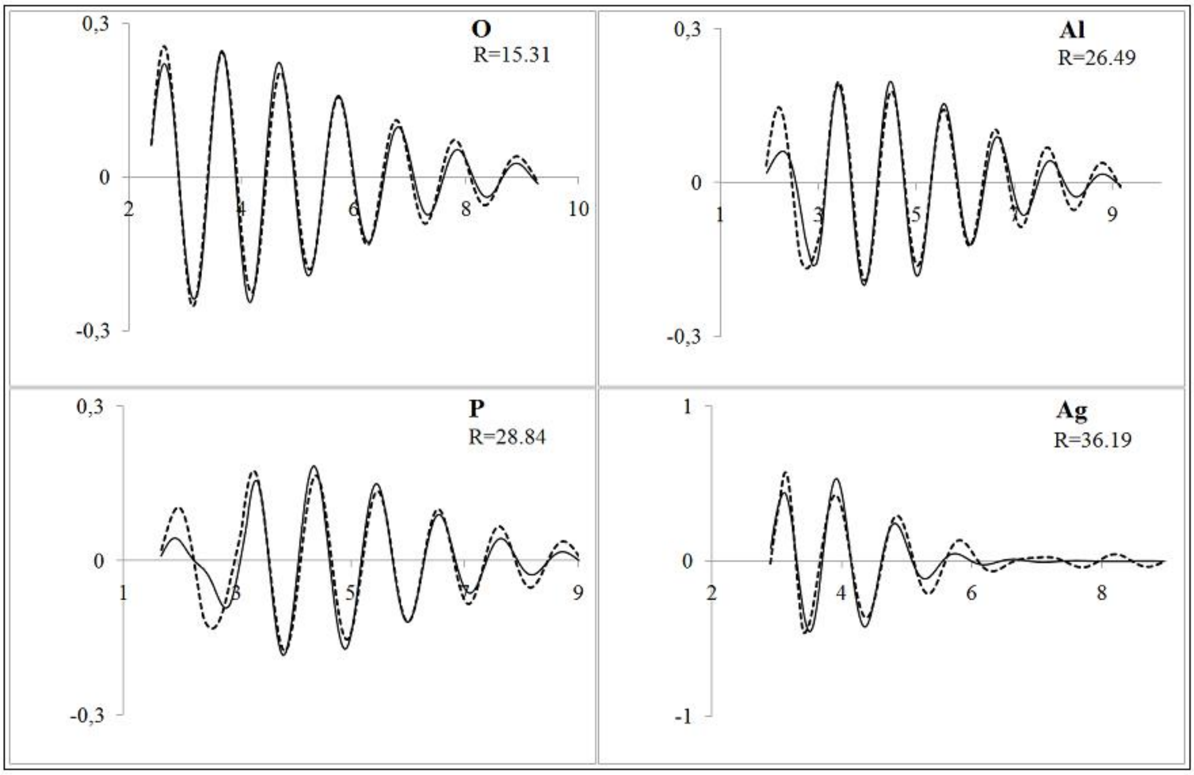

Figure 28: *Fourier Filtering of* $AgAPO_4$*-5/4c, with the R-values indicating the fit of the refinement.*

The Fourier Filtering shows that the second shell contains oxygen (lowest R-factor of 15.31). However the overall EXAFS of this sample could not be refined to a reasonable fit with chemically logical structural values when the second shell was set to be oxygen. Only when the second shell neighbours were set to be aluminium, did the overall spectrum give a good fit, with reasonable structural values and good R-factor. The Debye-Waller factors are a bit high, but this was the best result obtained for this sample. The ambiguous results make it difficult to draw conclusions about this sample. However, the fact that the other calcined samples have two separate oxygen shells, in addition to the shape of the XANES and the lack of silver neighbours, tells us that the silver(0) is not oxidized into silver(I) oxide, which is remarkable. The mechanism for silver cluster redispersion is not clear, however as silver(I) oxide is not formed we believe that the reoxidized silver(I) ions are bound to framework oxygen or water. Even though the APO_4-5 framework is ideally neutral, disordered sites can lead to extraframework aluminium or phosphorus functioning as Brønsted sites. Silver(I) ions may be fixed at these disordered sites, leading to a local environment similar to that of silver(I) sulphate. This may also explain the presence of the Al-shell in $AgAPO_4$-5/4c.

4.2.3 In-situ

Results from the *in-situ* experiments are shown in fig. 29 and 30. The *in-situ* calcination of $AgAPO_4$-5/4 confirms that the silver is oxidised during calcination, though not completely so in this experiment.

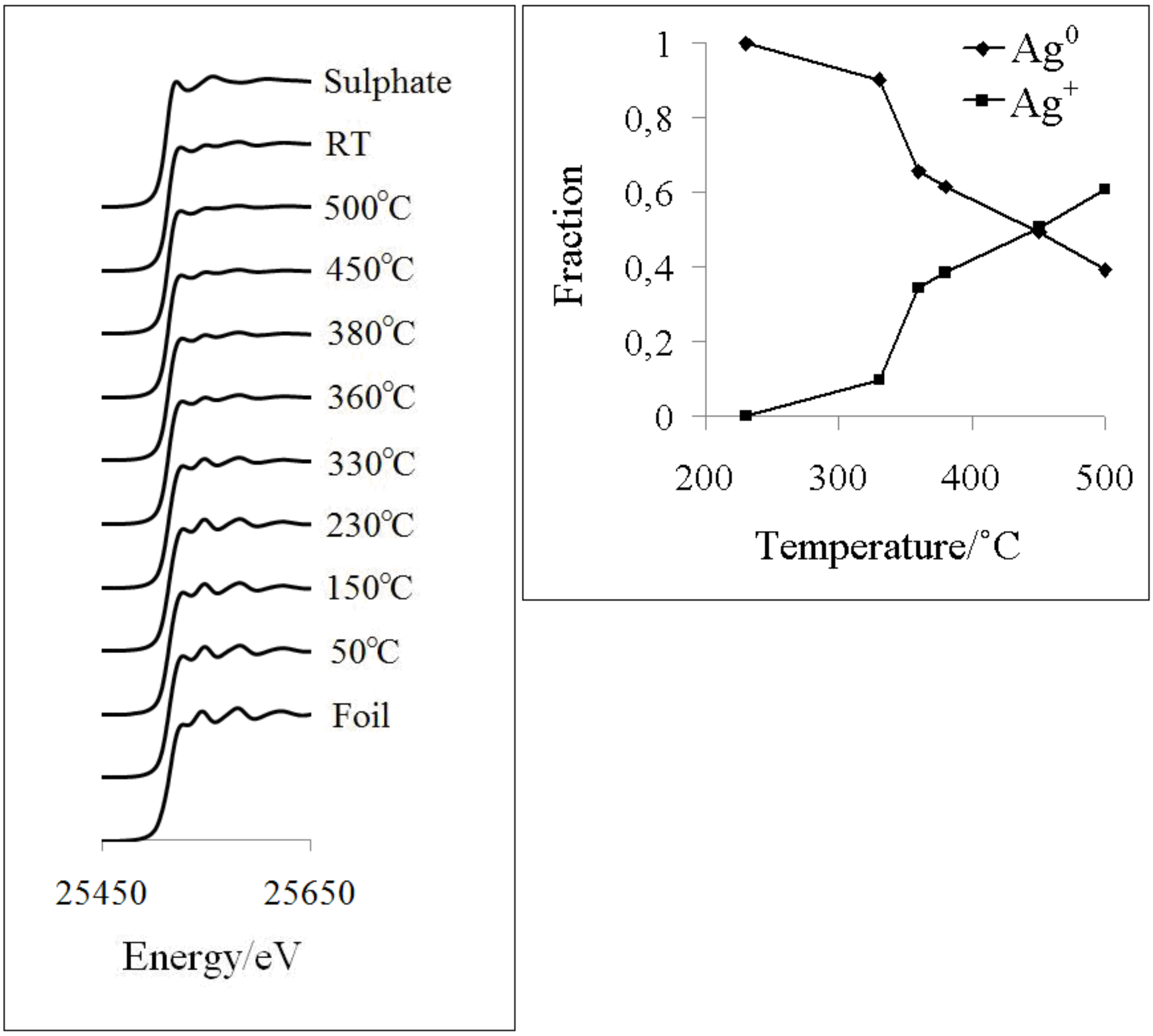

Figure 29: *Left: Normalized XANES of the calcination process, compared to silver(0) foil and silver(I) sulphate. Right: Linear combination fit of all the XANES from 330 ˚C (where the oxidation started) to 500 ˚C.*

The results of fig. 29 is that the oxidation of the silver starts at about 300°C, and in the end the treatment gives a sample containing ca 21 % silver(0) metal and ca 79 % silver (I) ions. These results are consistent with XRD, XANES and EXAFS results previously presented.

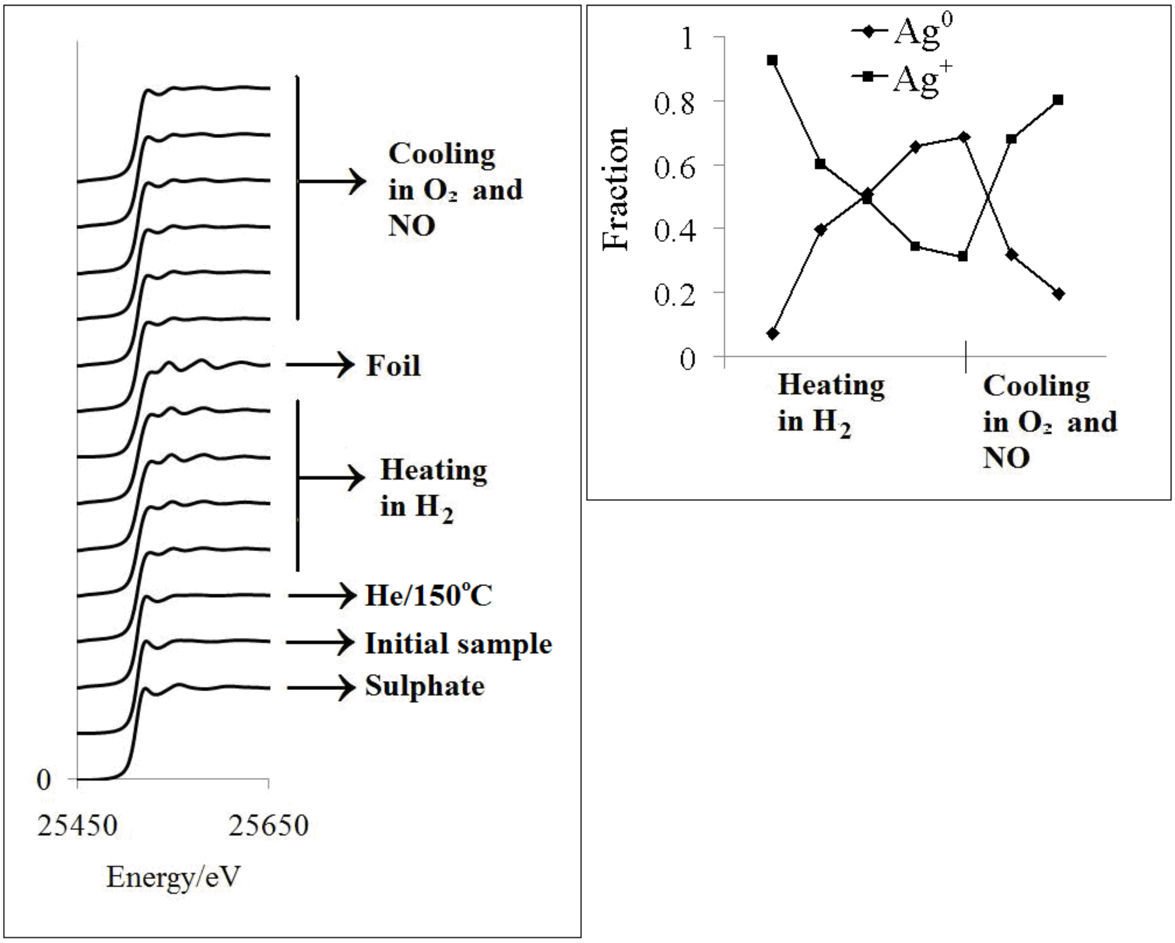

Figure 30: *Left: Normalized XANES of the redox process, compared to silver(0) foil and silver(I) sulphate. Right: Linear combination fit of all the XANES recorded in this process.*

In the second *in-situ* experiment, the Ag:SAPO-5 was exposed to a reducing environment, in order to investigate the formation of silver clusters. The reduction of the silver begins immediately as the hydrogen is put on (after treatment in He to 150°C), and the sample obtains a mixed environment of silver species. The completely heated sample (450°C) is compared to the foil, and the linear combination shows that this sample contains ca 69 % metallic silver and ca 31 % ionic silver. It can also be seen that the silver reoxidises immediately when the 50/50 mixture of oxygen and nitrogen monoxide is put on. The overall conclusion from the XANES and linear combinations is that the silver in Ag:SAPO-5 has reversible redox properties, which is interesting regarding catalysis. It would have been very interesting to test this sample on a deNOx rig, but this was not possible in this thesis.

The structural parameters obtained from refinements of the EXAFS recorded in the redox *in-situ* experiment are presented in table 6, and the visual results are displayed in fig. 31. The reduced silver(0) becomes dominant in the sample at 250°C/H_2, before this it is a mixed environment surrounding the silver, consistent with the XANES and the linear combination. As EXAFS only provide the average environment for all the silver species, the EXAFS and FT of the sample at 150°C looks like something between the initial ion exchanged sample and the reduced samples at higher temperatures with hydrogen.

Table 6: *Parameters from the least squares EXAFS analysis for the ion exchanged samples, and the in-situ EXAFS of Ag:SAPO-5. T= Al, Si, or P. RT=room temperature, after cooling in NO and O_2.*

Sample	**Shell**	**N**	**r/(Å)**	**$2\sigma^2$/(Å^2)**	**R/(%)**	**Ef**	**AFAC**	**Δk**
Ag:SAPO-11	Ag-O	2.4 (5)	2.34 (1)	0.020 (6)	28.90	-4.8 (5)	0.6865	2 – 9.7
	Ag···T	0.7 (6)	2.87 (1)	0.00 (2)				
	Ag···T	10 (3)	3.30 (2)	0.08 (2)				
Ag:SAPO-5	Ag-O	2.3 (4)	2.32 (1)	0.019 (5)	23.07	-3.0 (6)	0.6863	2 – 10
	Ag···T	1.9 (9)	2.88 (2)	0.02 (1)				
	Ag···T	8 (3)	3.21(2)	0.07 (2)				
Ag:SAPO-5 150°C/H_2	Ag-O	2.4 (3)	2.35 (1)	0.031 (3)	27.93	-3.4 (6)	0.6865	2.3 – 9.7
	Ag···T	0.65 (7)	2.421 (7)	0.001 (1)				
	Ag···T	7.1 (4)	3.247 (9)	0.035 (2)				
250°C/H_2	Ag-Ag	5.6 (6)	2.788 (7)	0.030 (2)	30.90	-2.7 (7)	0.65	2.2 – 10
350°C/H_2	Ag-Ag	9.2 (7)	2.803 (5)	0.034 (2)	23.66	-2.4 (4)	0.65	2.2 – 10
450°C/H_2	Ag-Ag	8.6 (8)	2.794 (6)	0.036 (2)	27.32	-2.0 (5)	0.65	2.2 – 10
RT	Ag-O	1.2 (2)	2.294 (8)	0.002 (4)	26.91	-4.7 (8)	0.6865	2 – 10
	Ag···T	1.9 (6)	2.91 (1)	0.007 (6)				
	Ag···T	11 (2)	3.25 (1)	0.046 (8)				

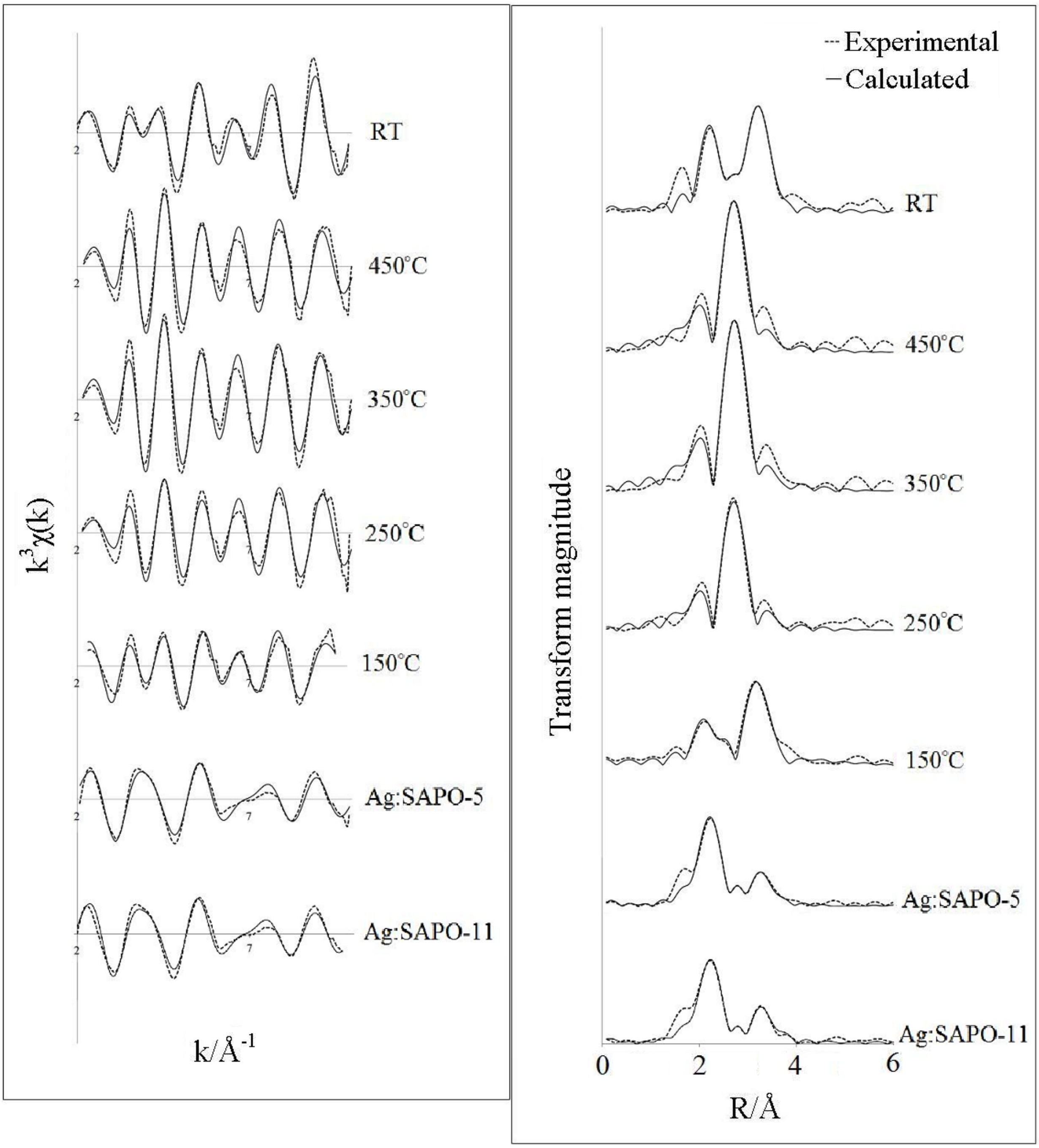

Figure 31: *Left: k^3-weighted EXAFS for the ion exchanged samples, and the different temperatures during redox in-situ of Ag:SAPO-5. Right: Experimental and calculated Fourier Transforms of the same samples.*

An interesting result here is the size of the clusters, which seem to be quite small, due to low multiplicity and short binding distance. It could have been expected to observe elongation of the binding distance, due to π-back bonding from the hydrogen molecules [25], but this is not the case. The low N- and r-values also suggests that the SAPO-5 framework stabilizes the clusters from migration and agglomeration to larger particles. The size of the *in-situ* clusters will also be further discussed in a later section.

The two ion exchanged samples, Ag:SAPO-5 and Ag:SAPO-11 have fairly similar multiplicities and binding distances, and their EXAFS's and FT's look similar in shape. But the two samples are quite different from the hydrothermally synthesised AgSAPO-11 and $AgAPO_4$-5's. This indicates that incorporation of silver by ion exchange gives the silver a different environment inside the framework, than do hydrothermal synthesis. This is also noticeable when comparing which elements that are neighbours of the silver. The general trend in the synthesised AgSAPO-11 and $AgAPO_4$-5's is the two independent shells of oxygen, but in the ion exchanged samples there are two of the T-atoms (Al, Si, or P) which are neighbours in shell 2 and 3. The neighbouring T-atoms indicate that silver is fixed at a cation site in the framework (which is expected). In addition, the low multiplicities and binding distances in the reduced state of Ag:SAPO-5 suggests that the silver clusters are trapped inside the pores of the microporous carrier, and thus are restricted from growing into bigger aggregates.

A feature that should be pointed out in this *in-situ* experiment is the Ag:SAPO-5/RT, which is the sample that had been heated in hydrogen and cooled in NO/O_2 and was back at room temperature when the EXAFS was recorded. The parameters from the refinements suggest that the silver goes back to the cation site where it was prior to the redox experiment, and is not oxidized into an oxide. This is a very interesting result, because it tells us that silver has reversible redox properties when ion exchanged into a SAPO framework, which was also the general conclusion from the XANES analysis of the *in-situ*. The results are consistent with Shimizu et al. (2007b), who report that the Ag^+ ions are fixed at cation sites in the zeolite (ZSM-5)[6], and that reduction in H_2 at 300°C yields Ag_4^{2+} clusters, which are redispersed into Ag^+ at cation sites upon reoxidation [44].

The multiplicities of the as-synthesised samples and the Ag:SAPO-5 in the *in-situ* experiment have been used to estimate the sizes of the clusters, and the number of silver atoms in the clusters. The estimated results are shown in fig. 32 and 33, and the numerical results from the estimates can be found in Appendix D. Even though the cluster sizes estimated from the multiplicities indicate that the clusters are too big to fit into the pores of the microporous carrier, the presence of smaller clusters cannot be excluded. As EXAFS only provide the average multiplicity of all the silver clusters present in a sample, there may be smaller silver(0) clusters present inside the framework, in addition to large clusters on the external surface of the particles of the microporous carrier. In the as-synthesised samples the

---

[6] ZSM-5 is an aluminiosilicate molecular sieve, and one of the most important molecular sieve catalysts in the petroleum industry [46].

clusters are probably mostly present on the external surface, as they are 27-128 Å in diameter. However in the *in-situ* experiment, the clusters may initially be inside the pores, and due to the heavy treatment at 450°C, they migrate out of the pores and grow larger on the external surface due to sintering.

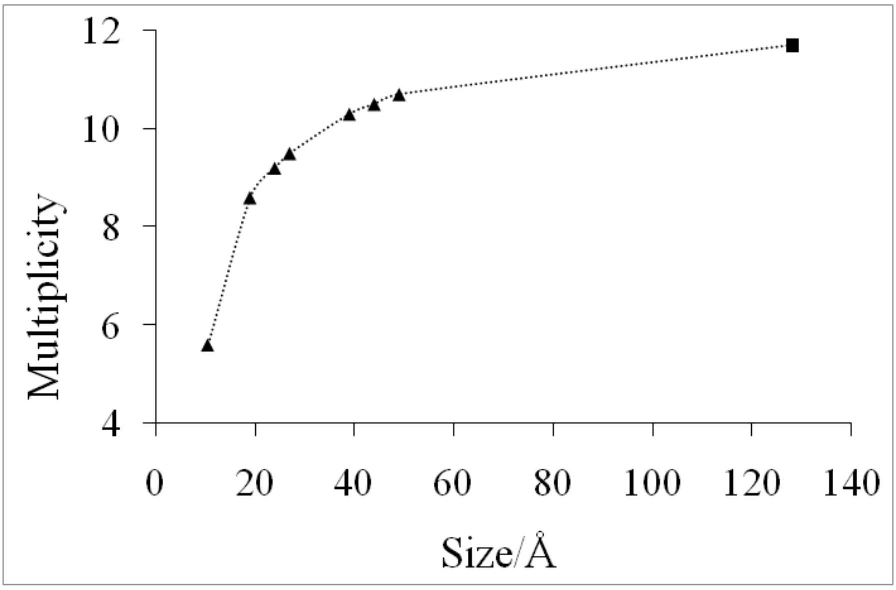

***Figure 32**: A plot showing the relationship between multiplicity and the size of the clusters. The sizes were obtained using figure 6, (chap. 2.3.1.). The point marked as ■ is not estimated with this method, as the size was not possible to estimate with fig. 6 due to too high multiplicity. The value of the cluster size for this sample (AgAPO$_4$-5/3) is the average size measured from the TEM images.*

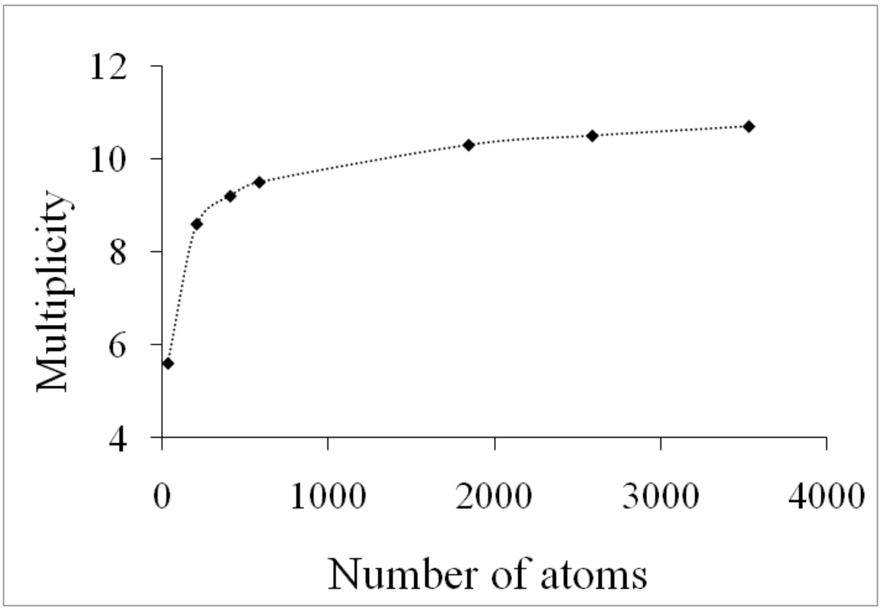

***Figure 33:** A plot of the values obtained using eq. 8, showing the relationship between multiplicity and number of atoms in the clusters. The value of AgAPO$_4$-5/3 is not included in this plot, due to too high value making the scale of the plot poor.*

The clusters are very small at 250°C in the *in-situ* of Ag:SAPO-5 in H_2, thus it would be interesting to investigate the catalytic properties of the silver nanoclusters at this temperature. Shimizu et al. (2007a; 2007b) found that adding hydrogen to the reaction mixture in selective catalytic reduction of NO_x by hydrocarbons (HC-SCR) in the presence of oxygen increased the rate of N_2 formation at 200°C (both in a Ag/Al_2O_3 catalyst, and silver ion exchanged ZSM-5). They found that the effect was due to presence of partially reduced silver clusters (Ag_4^{2+}), and they claim that monomeric silver(I) ions and metallic silver(0) clusters are inactive in the hydrogen promoted HC-SCR reaction [3; 44]. This shows that the state and morphology of the silver is crucial to the catalytic activity. In order to investigate the this effect in the Ag:SAPO-5, an *in-situ* EXAFS study with $NO + C_3H_8 + O_2 + H_2$ at 250°C could be performed, with a mass spectrometer measuring the exhaust of the possible reaction.

Conclusions

- It is not possible to incorporate silver(I) into the framework of APO_4-5 and SAPO-11 with hydrothermal synthesis; the silver(I) ions are reduced to metallic silver(0) prior to the crystallization of the framework, thus it cannot incorporate into the lattice.
- The clusters formed in the as-synthesised samples are too big to fit into the pores of the microporous carrier, thus they are believed to be present at the external surface of the particles of the APO_4-5's and SAPO-11.
- The silver(0) is oxidized during calcination, and the reoxidized silver(I) ions have a similar local environment as silver(I) sulphate, with two separate oxygen shells, and no silver shell, thus silver(I) oxide is not formed. Although the mechanism for silver(0) cluster redispersion is not clear, we believe the reoxidized silver(I) ions are bound to disordered sites of extraframework aluminium or phosphorus.
- The local environment of the ion exchanged silver(I) ions in Ag:SAPO-5 and AgSAPO-11 is different from that of the silver(I) in the calcined hydrothermally synthesised samples. The silver(I) is bound to two of the T atoms in the second and third shell, which indicate them being fixed at an acid site in the SAPO framework (which is expected). The differing environment of the silver points out that there is a significant difference between the two methods of introduction of silver into the framework, however the silver is in both cases in an extraframework position.
- The pores of the SAPO-5 restrict formation of large silver(0) clusters when a Ag:SAPO-5 is heated to 250°C in a reducing environment. Above this temperature the clusters become too large, and are probably present on the external surface. The average size of the nanoclusters at 250°C indicates that the clusters are too big to be inside the pores, however the existence of smaller clusters inside the pores cannot be excluded, as the EXAFS refinement only provide average multiplicity (and thus size) of all the clusters present, including larger clusters on the external surface.
- The silver in Ag:SAPO-5 possess reversible redox properties, and the silver(I) ions goes back to the cation sites upon reoxidation, and do not form silver(I) oxide.

Future work

- Perform new syntheses of $AgAPO_4$-5, AgSAPO-5 and AgSAPO-11, varying more parameters, such as longer crystallization at lower temperatures (e.g. 100°C for a week), and trying all the templates with all the different silver sources, with varying silver content in the syntheses.
- Perform the redox *in-situ* experiment on the Ag:SAPO-11, in the same manner as the experiment with Ag:SAPO-5, to be able to compare the ability of the SAPO framework to stabilize the clusters.
- Perform *in-situ* EXAFS experiments on ion exchanged Ag:SAPO-5 (and/or Ag:SAPO-11) with NO + C_3H_8 + O_2 + H_2 at 250°C, to investigate the activity and state of the silver in such an environment.
- Catalysis measurements of the samples in H_2 at 250°C.
- Perform Small Angle X-ray Spectroscopy (SAXS) to determine the size distribution of the silver nanoclusters.
- Collect TEM images of more samples, in order to compare the measured cluster sizes to the estimated results and find the cluster size distribution.
- Further investigation of the structure of silver(I) sulphate.

References

[1] Weckhuysen, B. M. (1999). Transition metal ions in microporous crytalline aluminophosphates: Isomorphous substitution. *European Journal of Inorganic Chemistry* (4), pp. 565-577.

[2] Hartmann, M., & Kevan, L. (2002). Substitution of transition metal ions into aluminophosphates and silicoaluminophosphates: characterization and relation to catalysis. *Research on Chemical Intermediates* (28), pp. 625-695.

[3] Shimizu, K., Tsuzuki, M., Kato, K., Yokota, S., Okumura, K., & Satsuma, A. (2007a). Reductive Activation of O2 with H2-Reduced Silver Clusters as a Key Step in the H2-Promoted Selective Catalytic Reduction of NO with C3H8 over Ag/Al2O3. *Journal of Physical Chemistry C* (111), pp. 950-959.

[4] Liu, Z.-P. J. (2004). Why is silver catalytivally active for NO reduction? A unique pathway via an inverted (NO)2 dimer. *Journal of the American Chemical Society* (126), pp. 7336-7340.

[5] Wichterlová, B. (2004). Structural analysis of potential active sites in metallo-zeolites for selective catalytic reduction of NOx. An attempt for the structure versus activity relationship. *Topics in Catalysis* (28), pp. 131-140.

[6] Montano, P. A., Zhao, J., Ramanathan, M., Shenoy, G. K., Schulze, W., & Urban, J. (1989). Structure of Silver Microclusters. *Chemical Physics Letters* (164), pp. 126-130.

[7] Wilson, S. T., Lok, B. M., Messina, C. A., Cannan, T. R., & Flanigen, E. M. (1982). Aluminophosphate Molecular Sieves: A New Class of Microporous Crystlline Inorganic Solids. *Journal of the American Chemical Society* (104), pp. 1146-1147.

[8] Hartmann, M., & Kevan, L. (1999). Transition-metal Ions in Aluminophosphate and Silicoaluminophosphate Molecular Sieves: Location, Interaction with Adsobates and Catalytic Properties. *American Chemical Society, Chemical Reviews* (99), pp. 635-663.

[9] Michalik, J., Azuma, N., Sadlo, J., & Kevan, L. (1995). Silver Agglomeration in SAPO-5 and SAPO-11 Molecular Sieves. *Journal of Physical Chemistry* (99), pp. 4679-4686.

[10] *Database of Zeolite Structures*. (2009). Retrieved April 10, 2009, from http://izasc.ethz.ch/fmi/xsl/IZA-SC/ft.xsl

[11] Gates, B. C. (1995). Supported metal clusters: synthesis, structure and catalysis. *American Chemical Society, Chemical Reviews* (95), pp. 511-522.

[12] Bailar, J. C., Emelèus, H. J., Nyholm, R., & Trotman-Dickenson, A. F. (1973). *Comprehensive Inorganic Chemistry* (1st ed.). Pergamon Press Ltd., ISBN:0-08-016988.

[13] Pauley, J. L., & Hau, H. H. (1966). Instability Constants of Silver-Amine Complexes in Isopropyl Alcohol. *Journal of Physical Chemistry* (70), pp. 3363-3366.

[14] George, K. C., & Abdulkhadar, M. (1992). Crystal Structure of Microclusters of Silver. *Crystal Research & Technology* (27), pp. 381-384.

[15] Xu, B., & Kevan, L. (1991). Formation of Silver Ionic Clusters and Silver Metal Particles in Zeolite Rho Studied by Electron Spin Resonance and Far-Infrared Spectroscopies. (95), pp. 1147-1151.

[16] Shimizu, K., Shibata, J., Yoshida, H., Satsuma, A., & Hattori, T. (2001). Silver-Alumina catalysts for selective reduction NO by higher hydrocarbons: structure of active sites and reaction mechanisms. *Applied Catalysis B: Enviromental* (30), pp. 151-162.

[17] Shibata, J., Shimizu, K., Takada, Y., Shichi, A., Yoshida, H., Satokawa, S., et al. (2004). Structure of active Ag clusters in Ag zeolites for SRC of NO by propane in the presence of hydrogen. *Journal od Catalysis* (227), pp. 367-374.

[18] Teo, B. K. (1986). *EXAFS: Basic Principles and Data Analysis.* Springer-Verlag, ISBN: 3-540-15833-2.

[19] Fay, M. J., Proctor, A., Hoffmann, D. P., & Hercules, D. M. (1988). Unraveling EXAFS Spectroscopy. *Analytical Chemistry* (60), pp. 1225-1243.

[20] *ESRF Website.* (2009). Retrieved April 7, 2009, from http://www.esrf.eu/UsersAndScience/Experiments/CRG/BM01/bm01b

[21] *Athena Website.* (2009). Retrieved April 7, 2009, from file:///C:/Program%20Files/Ifeffit/share/aug/html/index.html

[22] Murphy, L. M., & Charnock, J. M. (2009). *EXCURV98: Getting started - a brief introduction to EXAFS analysis.* Retrieved April 7, 2009, from http://www.srs.dl.ac.uk/xrs/courses/exafs_anal02.htm

[23] deGraaf, J., van Dillen, A. J., de Jong, K. P., & Koningsberger, D. C. (2001). Preparation of Highly Dispersed Pt Particles in Zeolite Y with a Narrow Particle Size

Distribution: Characterisation by Hydrogen Chemistorption, TEM, EXAFS Spectroscopy and Particle Modeling. *Journal of Catalysis* (203), pp. 307-321.

[24] Penner-Hahn, J. E. (1999). X-ray absorption spectroscopy in coordination chemistry. *Coordination Chemistry Reviews* (190-192), pp. 1101-1123.

[25] Atkins, P., Overton, T., Rourke, J., Weller, M., & Armstrong, F. (2006). Inorganic Chemistry, 4th edition. *Oxford University Press* (ISBN: 0-19-926463-5).

[26] Skoog, D. A., West, D. M., Holler, F. J., & Crouch, S. P. (2004). *Fundamentals of Analytical Chemistry* (8th ed.). Brooks/Cole of Thompson Learning Inc., ISBN-10: 0-534-41797-3.

[27] Croft, W. J. (2006). *Under the Microscope: A brief History of Microscopy*. World Scientific Co. Pte. Ltd., ISBN: 981-02-3781-2.

[28] Ramachandran, V. S., & Beaudoin, J. J. (2001). *Handbook of Analytical Techniques in Concrete Science and Technology*. William Andrew Publishing/Noyes, ISBN: 978-0-8155-1437-4.

[29] Muños, T., Prakash, A. M., Kevan, L., & Balkus Jr., K. J. (1998). Synthesis and Characterisation od CuAPO-5 Molecular Sieves: Evidence for the Framework Incorporation of Cu(II) Ions. *Journal of Physical Chemistry* (102), pp. 1379-1386.

[30] Lee, C. W., Chen, X., & Kevan, L. (1991). Electron Spin Resonance and Electron Spin Echo Modulation Studies of Cupric Ions Location and Adsorbate Interactions in the Cu2+-Exchanged H-SAPO-11 Molecular Sieve. *Journal of Physical Chemistry* (95), pp. 8626-8632.

[31] Lok, B. M. (1984). Silicoaluminophosphate Molecular Sieves: Another New Class of Microporous Crytalline Inorganic Solids. *Journal of the American Chemical Society* (106), pp. 6092-6093.

[32] Bontempi, E., Colombi, P., Depero, L. E., Cartechini, L., Presciutti, F., Brunetti, B. G., et al. (2006). Glancing-incidence X-ray diffraction of Ag nanoparticles in gold lustre decoration of Italian Renaissance pottery. *Applied Physics A* (83), pp. 543-546.

[33] You, T., Xu, S., Sun, S., & Song, X. (2009). Controllable synthesis of pentagonal silver nanowires via a simple alcohol-thermal method. *Material Lettes* (63), pp. 920-922.

[34] Gläser, R., & Laha, S. C. (2007). The role of extra-framework chromium species for the catalytic activity of [Cr]APO-5-type materials. *Catalysis Communications* (8), pp. 91-96.

[35] Oliveira, A. C., Essayem, N., Tuel, A., Clacens, J.-M., & Taarit, Y. B. (2008). Studies on MeAPSO-5: An investigation of physiochemical and acidic properties. *Catalysis Today* (133-135), pp. 56-62.

[36] Xiong, J., Ding, Y., Zhu, H., Yan, L., Lui, X., & Lin, L. (2003). Nitrogen-Incorporated SAPO-11 Molecular Sieve: Synthesis, Characterization and Properties. *Journal of Physical Chemistry* (107), pp. 1366-1369.

[37] Shengzhen, Z., Sheng-Li, C., Peng, D., Zhiyong, J., Junying, Z., & Keqi, X. (2007). Synthesis, characterization and hydroisomerization catalytic performance of nanosize SAPO-11 molecular sieves. *Catalysis Letters* (118), pp. 109-117.

[38] Poldán, R., Sánchez-Sánches, M., Sankar, G., Romero-Salguero, F. J., & Jiménez-Sanchidrián, C. (2007). Influence of pH and Si content on Si incorporation in SAPO-5 and their catalytic acitivity for isomerisation of n-heptane over Pt loaded catalysts. *Microporous and Mesoporous Materials* (99), pp. 288-298.

[39] Gao, Q., Chen, J., Li, S., & Xu, R. (1996). Synthesis and characterization of aluminophosphate molecular sieve AlPO4-41 from alcohol systems. *Microporous Materials* (7), pp. 219-223.

[40] Houde-Walter, S. N., Inman, J. M., Dent, A. J., & Greaves, G. N. (1993). Sodium and silver environments and ion-exchange processes in silicate and aluminosilicate glasses. *Journal of Physical Chemistry* (97), pp. 9339-9336.

[41] Levy, H. L., & Lisensky, G. C. (1978). Crystal structures of sodiumsulphate decahydrate (Glauber's salt) and sodium tetraborate decahydrate (Borax). Redetermination by Neutron Diffraction. *Acta Crystallographia Section B: Structural Sciences* (34), pp. 3502-3510.

[42] Robbins, D. J., & Day, P. (1977). Why is silver chromate red? The 4.2 K polarized electronic spectrum of chromate in silver sulphate. *Molecular Physics* (34), pp. 893-898.

[43] Rayner-Canham, G. O. (2003). *Descriptive Inorganic Chemistry* (3rd ed.). W. H. Freeman and Company, ISBN: 0-7167-4620-4.

[44] Shimizu, K., Sugino, K., Kato, K., Yokota, S., Okumura, K., & Satsuma, A. (2007b). Reaction Mechanism of H2-Promoted Selective Catalytic Reduction of NO with C3H8 over Ag−MFI Zeolite. *Journal of Physical Chemistry* (111), pp. 6481-6487.

[45] Chao, K. J., Wei, A. C., Wu, H. C., & Lee, J. F. (1999). Characterisation of metal-incorporated molecular sieves. *Catalysis Today* (49), pp. 277-284.

[46] Xu, r. P. (2007). *Chemistry of zeolites and related porous materials: synthesis and structure*. Wiley-Interscience, ISBN: 0470822333.

Appendix A

Mass Spectrogrames

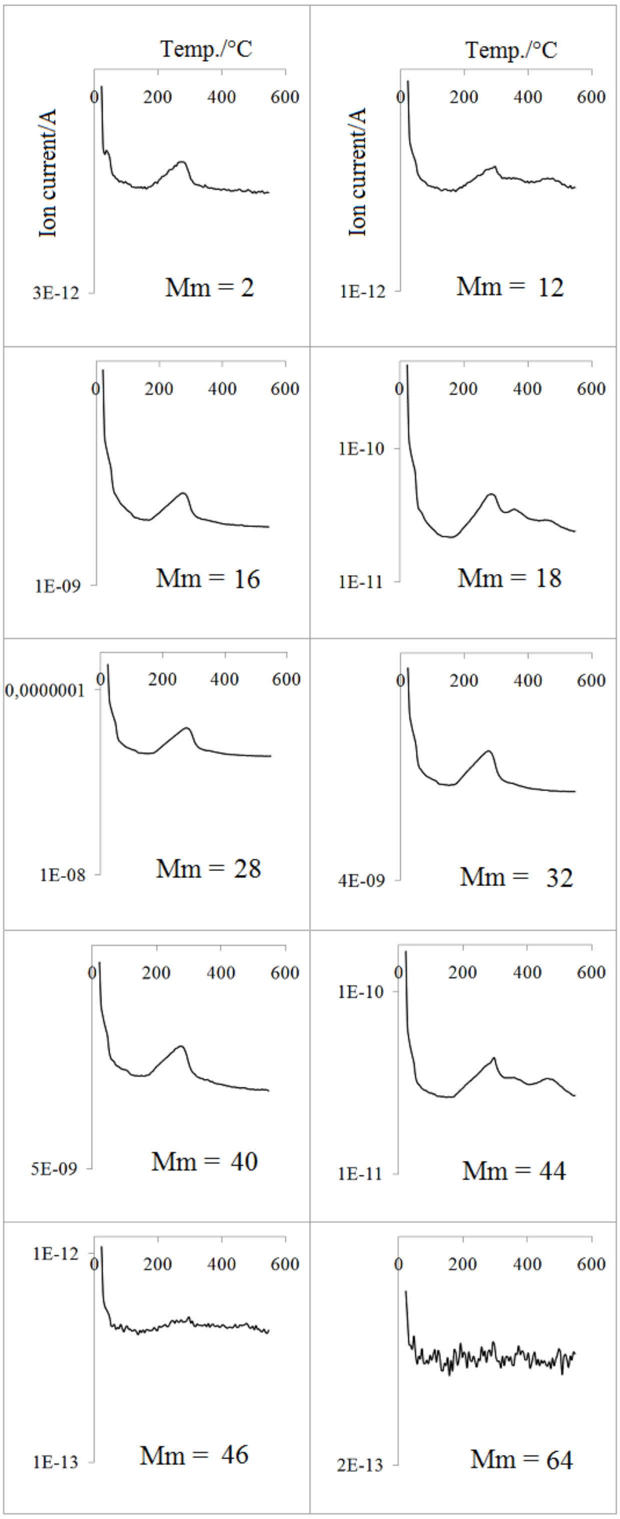

Figure A1: *The results of the mass spectrometry measurements during TGA of AgSAPO-11*

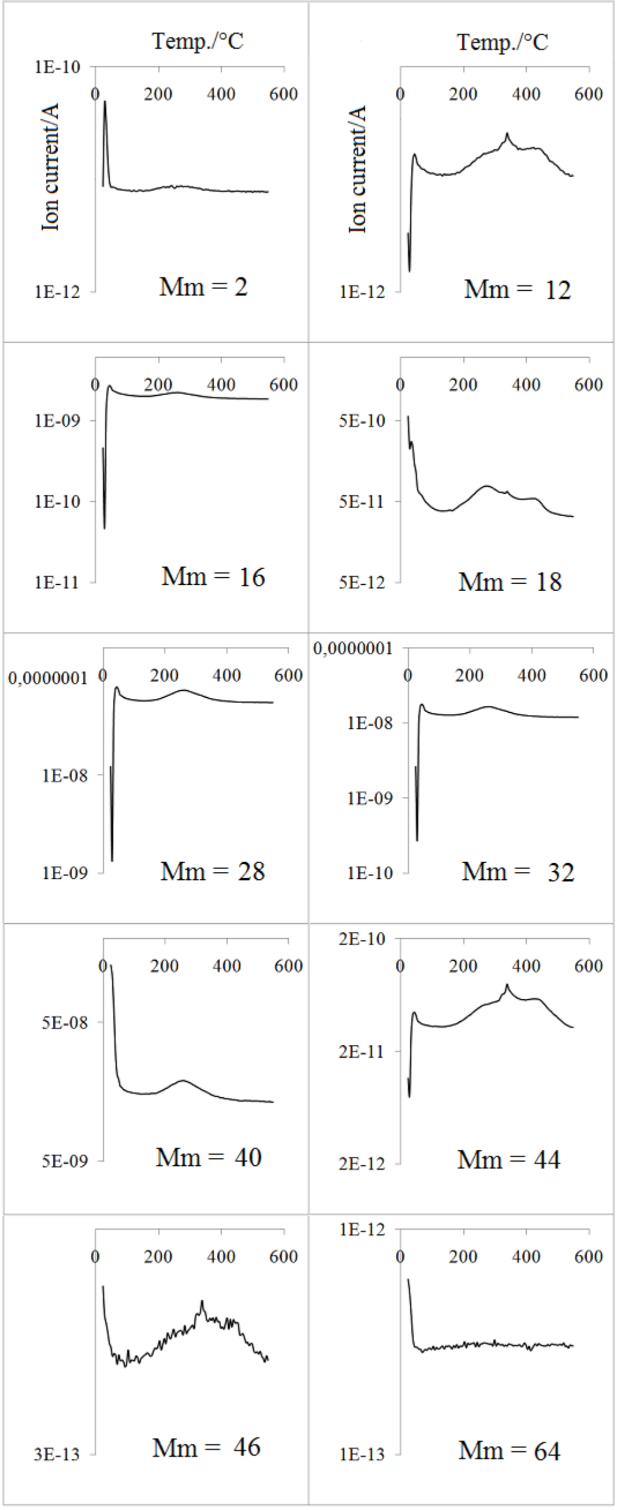

Figure A2: *The results of the mass spectrometry measurements during TGA of* $AgAPO_4$*-5.*

Appendix B

Linear combination

Table B: *Percentage of ionic (Ag^+) and metallic (Ag^0) silver species in the samples, found by linear combination fit in* `Athena`*, comparing them to sulphate and foil.*

Sample	**% ionic**	**% metallic**
$AgAPO_4$-5/1a	19.4	80.6
$AgAPO_4$-5/2a	25.4	74.6
$AgAPO_4$-5/3a	21.9	78.1
$AgAPO_4$-5/4a	17.1	82.9
AgSAPO-11a	21.2	78.8
$AgAPO_4$-5/1c	100	0
$AgAPO_4$-5/2c	100	0
$AgAPO_4$-5/3c	100	0
$AgAPO_4$-5/4c	100	0
AgSAPO-11c	100	0

Appendix C

Fourier Filtering

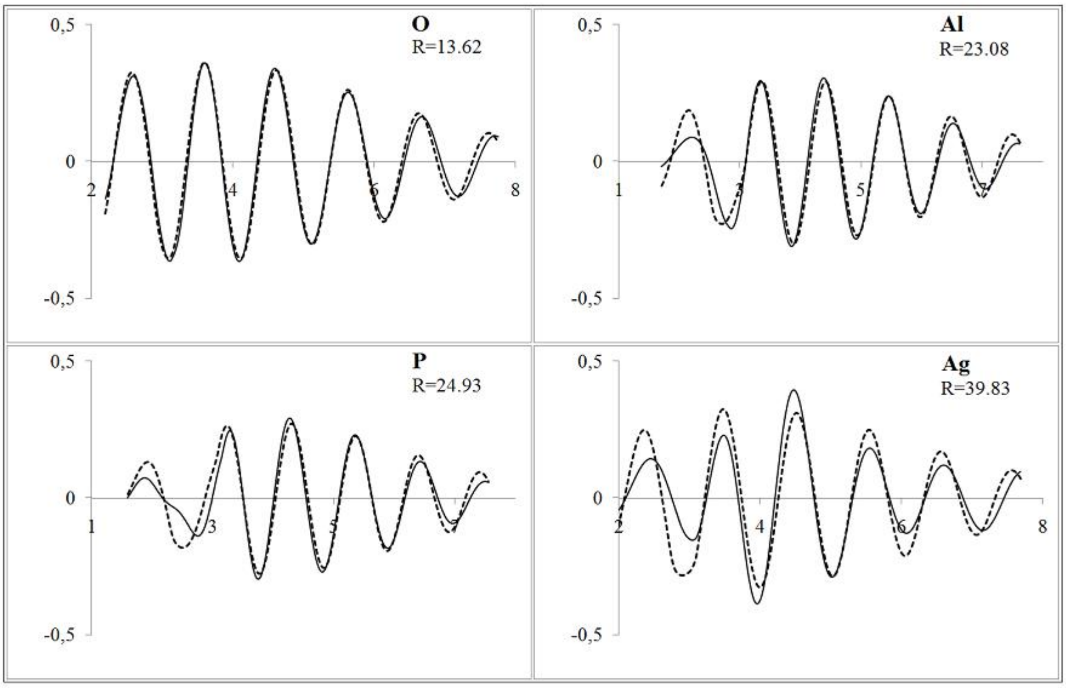

Figure C1: *Fourier Filtering of the second shell of AgAPO$_4$-5/1c*

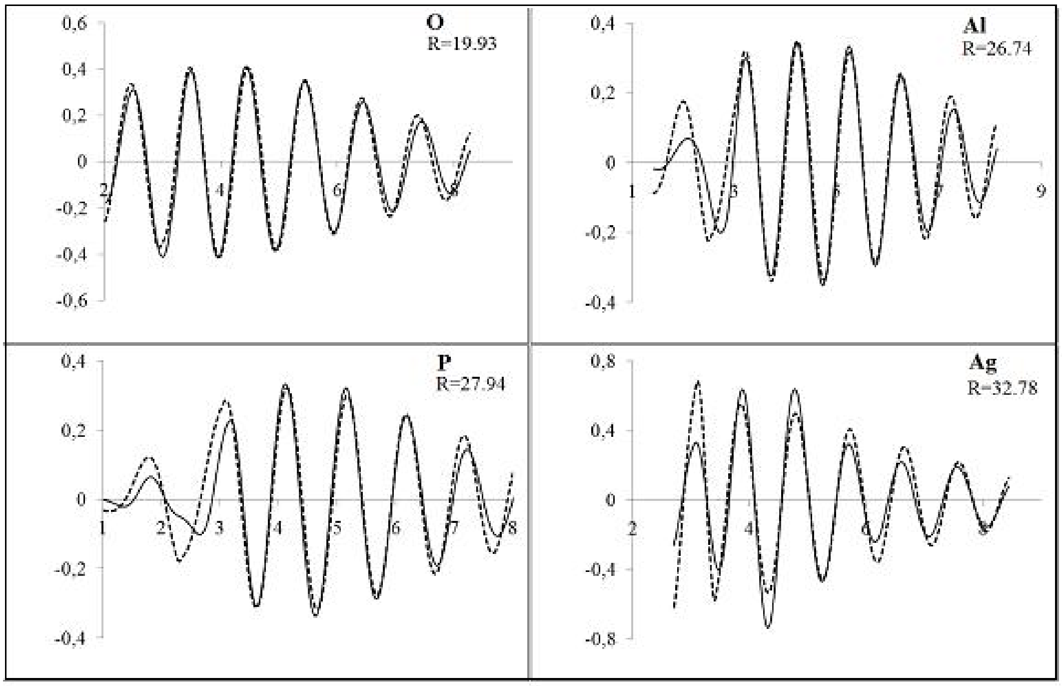

Figure C2: *Fourier Filtering of the second shell of AgAPO$_4$-5/2c*

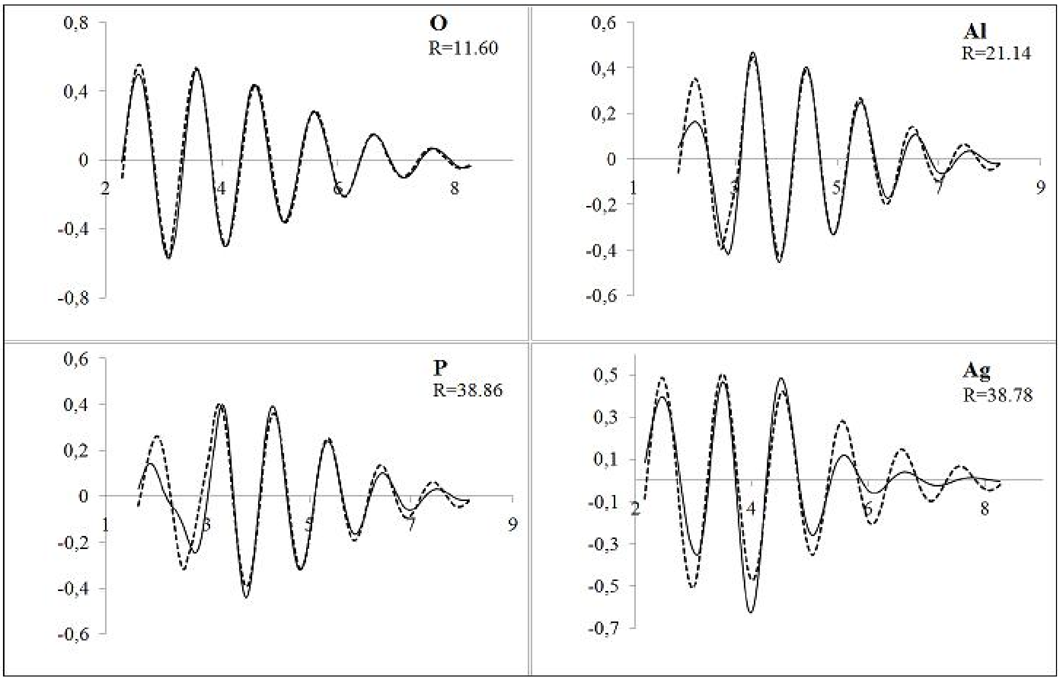

Figure C3: *Fourier Filtering of the second shell of AgAPO$_4$-5/3c*

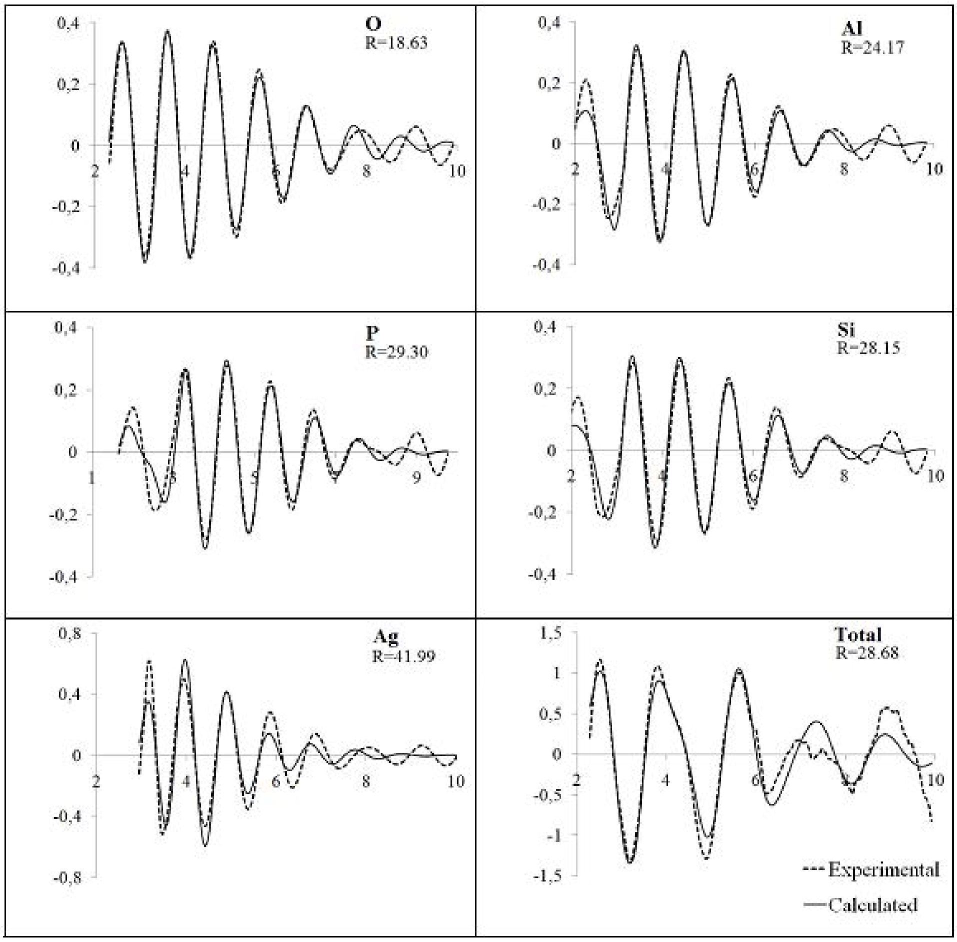

Figure C4: *Fourier Filtering of the second shell of AgSAPO-11c*

Appendix D

Size of clusters

Table D:* Numerical values from the estimation of size and number of atoms in the clusters using the plot from deGraaf [23] (size) and eq. 8 in chap. 2.3.1.*

Sample	**N**	**Size/Å**	**Number of atoms**
$AgAPO_4$-5/1a	10.7	49	3532
$AgAPO_4$-5/2a	10.3	39	1845
$AgAPO_4$-5/3a	11.7	*128*[1]	63729
$AgAPO_4$-5/4a	10.5	44	2589
AgSAPO-11a	9.5	27	585
AgSAPO-5/250°C/H_2	5.6	10.5	35
AgSAPO-5/350°C/H_2	9.2	24	410
AgSAPO-5/450°C/H_2	8.6	19	208

[1] *Average value from TEM images, and not obtained from the plot.*